

Multiplicity of Massive stars in the Milky Way (M³W).

I. Project description, UNWIND, application to GLS 11 448, and DIB catalog

J. Maíz Apellániz¹, R. C. Gamen^{2,3}, G. Holgado^{4,5}, S. Rosu⁶, J. I. Arias⁷, S. Simón-Díaz^{4,5}, A. Pellerin⁸, M. Abdul-Masih^{4,5}, E. Madero Fuentes^{1,9}, J. A. Molina-Calzada^{1,9}, and R. H. Barbá^{*}

¹ Centro de Astrobiología, CSIC-INTA. Campus ESAC. C. bajo del castillo s/n. E-28 692 Villanueva de la Cañada, Madrid, Spain. e-mail: jmaiz@cab.inta-csic.es

² Instituto de Astrofísica de La Plata, CONICET-UNLP. Paseo del Bosque s/n. La Plata, Argentina.

³ Facultad de Ciencias Astronómicas y Geofísicas, UNLP. Paseo del Bosque s/n. La Plata, Argentina.

⁴ Instituto de Astrofísica de Canarias. E-38 200 La Laguna, Tenerife, Spain.

⁵ Departamento de Astrofísica, Universidad de La Laguna. E-38 205 La Laguna, Tenerife, Spain.

⁶ Département d’Astronomie, Université de Genève. Chemin Pegasi 51. CH-1290, Versoix, Switzerland.

⁷ Departamento de Astronomía, Universidad de La Serena, Av. Juan Cisternas 1200 Norte. La Serena, Chile.

⁸ Department of Physics and Astronomy, SUNY Geneseo. Geneseo, NY 14 454, United States of America.

⁹ Departamento de Astrofísica y Física de la Atmósfera. Universidad Complutense de Madrid. E-28 040 Madrid, Spain.

Received 2 April 2026; accepted YY ZZZ 2026

ABSTRACT

Context. Multiplicity is ubiquitous among massive stars and its understanding is constrained by the limited sample of well-determined orbits. This hampers the progress of astronomical fields ranging from the initial mass function to gravitational-wave sources.

Aims. The immediate goal of Multiplicity of Massive stars in the Milky Way (hereafter, M³W) is to significantly increase the number of massive multiple systems with well-determined orbits and masses. With that information in hand, we will address issues such as multiplicity statistics, the mass function in clusters and the field, the properties of binaries with compact companions and gravitational-wave progenitors, the origin and characteristics of runaways and their 3-D motions, the use of apsidal motion as a probe of stellar interiors, and the mass discrepancy between different methods (evolutionary, spectroscopic, and Keplerian).

Methods. In this first paper, we present the project: describe the data and tools that will be used, including the disentangling UNWIND tool; analyse the very massive twin binary system GLS 11 448; and briefly introduce some of the following papers of the series.

Results. We present a new orbital solution for GLS 11 448, using UNWIND to obtain for the first time disentangled spectra for the full 3820-11 000 Å range for an OB spectroscopic binary. We derive the stellar parameters and present how UNWIND makes new stellar lines available for the study of O stars. The Aa and Ab components of GLS 11 448, both classified as O3.5 II(f*), are the two most massive O stars ever detected according to the evolutionary masses of $70 \pm 10 M_{\odot}$ and $76 \pm 11 M_{\odot}$ determined in this paper. We also report the first-ever detection of the interstellar He I $\lambda 10 830$ triplet in absorption in an OB-star sightline. As a by-product of the interstellar-medium model derived for UNWIND using GLS 11 448 and five other standard stars, we present the most detailed diffuse-interstellar-band (DIB) library ever built, with a total of 631 DIBs in the 4000-17 100 Å range, of which 37 are fitted with multiple-Gaussian profiles and 119 had never been identified before.

Key words. Binaries: eclipsing — Binaries: spectroscopic — Binaries: visual — Stars: massive — Stars: individual: GLS 11 448 — ISM: lines and bands

1. Introduction

It has been known for several decades that massive stars have a high degree of multiplicity. The first large-scale systematic study of massive-star multiplicity was that of Mason et al. (1998). Sota et al. (2014) showed that few (if any) massive binaries are born in single systems and Maíz Apellániz et al. (2019b) that triple- and higher-order systems are even more common than regular binaries. Massive-star multiplicity is a blessing because it allows to determine component masses and other characteristics, but is also a curse because it complicates the understanding of star formation and the determination of mass functions. Furthermore, a large fraction of stars in multiple systems are close enough to mutually influence their evolution (Sana

et al. 2012) and, eventually, their end products, making massive-star multiplicity one of the determining factors in the dynamical and chemical evolution of galaxies.

Our group has been involved in massive-star surveys for the last two decades. The Galactic O-Star Spectroscopic Survey (GOSSS, Maíz Apellániz et al. 2011) started with the main purpose of obtaining intermediate-resolution spectroscopy of as many O stars as possible but we soon discovered its usefulness for identifying multiple systems that could be studied through other means (Sota et al. 2014). In parallel, we also started OWN as a multi-epoch high-resolution spectroscopic survey of massive stars in the southern hemisphere (Barbá et al. 2010, 2017) specifically oriented towards spectroscopic multiplicity. In the northern hemisphere several spectroscopic (NoMaDS, Maíz Apellániz et al. 2012; CAFÉ-BEANS, Negueruela et al.

* Deceased.

2015; IACOB, Simón-Díaz et al. 2011b) and high-resolution imaging (Maíz Apellániz 2010) surveys converged into an OWN-equivalent project, MONOS (Multiplicity Of Northern O-type Stars, Maíz Apellániz et al. 2019b). The large amount of epochs generated by those projects coupled with the availability of spectroscopic databases led to the creation of LiLiMaRlin (Library of Libraries of Massive-star high-Resolution spectra, Maíz Apellániz et al. 2019a) in order to uniformly process the currently $\sim 10^5$ such epochs of hot (mostly massive) stellar high-resolution spectroscopic data.

Both OWN and MONOS have been highly successful. OWN required an extended time span before the publication of its first comprehensive results, primarily to secure a sufficient number of epochs to properly constrain long-period orbits. The project was also affected by the unexpected passing of its Principal Investigator, Rodolfo Barbá, in late 2021. In 2026 the first paper on 23 SB1 orbits has been accepted (Barbá et al. 2026, OWN I) and a second paper on SB2 orbits will be submitted soon (Gamen et al. in prep., OWN II). Yet, OWN results on individual stars had already appeared as separate papers (Gamen et al. 2006, 2008, 2015a,b; Arias et al. 2010; Campillay et al. 2019; Barbá et al. 2020; Putkuri et al. 2021, 2022, 2023; Ansín et al. 2023). MONOS has produced three papers: MONOS I on the multiplicity statistics of northern O-type systems (Maíz Apellániz et al. 2019b), MONOS II with 35 SB1 orbits (Trigueros Páez et al. 2021), and MONOS III with 10 SB2E orbits (Holgado et al. 2025b).

As OWN and MONOS have run their courses in the last years, we decided to continue them with the new project presented in this paper, Multiplicity of Massive stars in the Milky Way (M³W). The main reason for a follow-up project is that, despite the advances provided by the two projects (and by those of other groups, see next section), we have only scratched the surface of the problem of massive-star multiplicity and its main objectives are not yet solved. M³W gets rid of the northern-southern hemisphere separation of the previous projects (which made sense previously, when spectroscopic archives were scarce in data, but not so much currently), the limitations of the OWN sample, and of the restriction to O (and WN) stars by including other types of massive stars. It is a timely project because of the incoming availability of epoch astrometry and spectroscopy with *Gaia* DR4 in late 2026 (Prusti et al. 2016) and of ground-based multi-fibre spectroscopic surveys such as WEAVE (Jin et al. 2024) and 4MOST (de Jong et al. 2019). It will also make use of the tools we have developed for OWN and MONOS, such as UNWIND (presented in this paper but already used in OWN I and MONOS III), that will allow us for a more productive exploitation of the data.

This paper is organised as follows. First, we describe the project, second we present the UNWIND tool, third we apply it to a benchmark SB2 system, GLS 11 448, and we finish the main section of the paper with a summary and an outlook of the incoming papers of the series. A short Appendix provides a glossary of terms and a longer one presents the DIB catalog generated for UNWIND.

2. Project description

2.1. Objectives

The immediate goal of M³W is to determine the kinematical and dynamical properties (systemic or centre-of-mass velocity, orbital parameters, mass, and k_2 internal structure constant, Rosu 2025) of as many Galactic massive stars as possible. Such indi-

vidual analyses are a necessary step before any subsequent ones on the collective properties because systemic velocities of massive stars are frequently biased (an issue that will be explored in a paper of the M³W series) and some published orbits are either contaminated by third-light effects or even false orbits generated by e.g. poor temporal sampling of pulsating stars (MONOS II, Simón-Díaz et al. 2024). Furthermore, massive stars are scarce so any additional information about one or several objects may be crucial to solve problems relevant to a class.

Beyond determining individual characteristics, the next goal of M³W is to determine the multiplicity of massive stars in the solar neighbourhood (within a few kpc of our Galactic position). There are analyses on the spectroscopic multiplicity of massive stars in Galactic clusters (Sana et al. 2008, 2009, 2011; Kobulnicky et al. 2014; Banyard et al. 2022) but those are limited in sample size and scope. Furthermore, for a complete understanding of massive-star multiplicity, one needs to include the effect of longer-period systems (Maíz Apellániz 2010; Sana et al. 2014). Spectroscopic studies with larger samples have been done in the Magellanic Clouds (Sana et al. 2013; Dunstall et al. 2015; Almeida et al. 2017; Shenar et al. 2024; Britavskiy et al. 2025; Villaseñor et al. 2025; Sana et al. 2025) which inform us of the metallicity dependence. Yet, at those distances our knowledge of multiplicity is limited by spatial resolution, hence limiting our understanding of its behaviour at large separations. Those limitations are the reason for expanding the sample of over 100 O-type orbits in the solar neighbourhood carried out by OWN and MONOS into a larger volume-limited sample containing several hundreds of massive stars with M³W, leading to a thorough study of massive-star multiplicity in our nearby Galactic environment.

Those individual and collective analyses of the motion of massive stars will yield subsequent studies with different objectives. The first one will be the analysis of massive binaries with compact progenitors, expected to become gravitational-wave sources, for which we will combine our spectroscopic data with *Gaia* DR4 epoch astrometry to derive accurate masses. Another direct application will be the use of long time baselines to determine the apsidal motion of eccentric binaries and in that way probe their stellar interiors (Rosu 2022; Rosu et al. 2020a,b, 2022a,b). The determination of accurate Keplerian stellar masses, solving the inclination problem with eclipses or astrometry, should address the discrepancies between evolutionary and spectroscopic masses, still (crazily) present after all these years (Herrero et al. 1992; Herrero 2007; Holgado et al. 2020, 2025a). This, in turn, should lead to the necessary corrections in the massive-star mass function due to hidden multiplicity (Maíz Apellániz 2008) and other issues related to binary interactions, such as the stars expelled from clusters as runaways (Maíz Apellániz et al. 2022). Runaway stars are another field that will be impacted by M³W, for example by the derivation of more accurate systemic velocities that should allow a better backtracing of Galactic trajectories and by the detection of hidden companions to elucidate their formation mechanisms (Maíz Apellániz et al. 2018b; Carretero-Castrillo et al. 2023).

These objectives constitute the primary motivation for this project. Additional goals are expected to emerge during its execution, including the study of specific systems of interest that may exhibit unique characteristics.

2.2. Data

Sample. The samples for OWN and MONOS were built from the Galactic O-Star Catalog (GOSC, Maíz Apellániz et al. 2004; Sota et al. 2008) which started as a compilation of high-quality

spectral classifications of O stars from Walborn (1972, 1973, 1982) and was later expanded to include the results of GOSSS and other types of massive stars (massive B stars, WRs...). For M³W we will use the more extensive Alma Luminous Star (ALS) catalog, which also started as a literature compilation (Reed 2003) but was later cross-matched with *Gaia* and expanded with additional sources (Pantaleoni González et al. 2021, 2025). ALS gives us access to a significantly larger sample of Galactic massive stars ($\sim 15\,000$) that will soon be expanded by an order of magnitude using a systematic search with *Gaia* data (Maíz Apellániz et al. in prep.) and an extension into the Magellanic system (Molina Calzada & Maíz Apellániz 2025).

LiLiMaRlin. The bulk of the M³W spectroscopic data, at least in the first years of the project will be the LiLiMaRlin high-resolution spectroscopy (Maíz Apellániz et al. 2019a), which is uniformly processed and already adapted to the UNWIND needs (see Sect. 3). We have already collected $\sim 10^5$ epochs from database searches (such as ESO and OHP) and our own programs at ORM, CAHA, and ESO. In the incoming years we will continue adding high-resolution spectra in both ways.

Additional ground-based spectroscopy. High-resolution spectroscopy ($R > 10\,000$) is the best adapted for the analysis of spectroscopic binaries. However, intermediate-resolution ($R = 2000 - 10\,000$) spectroscopy can suffice for large velocity amplitudes¹. Furthermore, high-resolution spectra are usually obtained with a single circular aperture that (for the most part) erases the spatial information from visual binaries (e.g. Simón-Díaz et al. 2015), something that can be overcome at lower spectral resolutions with long slits or IFUs (Maíz Apellániz et al. 2018a, 2021b; Maíz Apellániz & Barbá 2020). We expect to include in M³W intermediate-resolution spectra from GOSSS, WEAVE (Jin et al. 2024), 4MOST (de Jong et al. 2019), and possibly other ground-based sources.

Gaia astrometry and spectroscopy. The most useful new contribution of *Gaia* DR4 to M³W will be the epoch astrometry, which will allow for the full orbital determination of massive stars with a compact companion, where the photocentre corresponds to the visible stars, and the placement of constraints for systems with a significant magnitude difference between the two components. We note, however, the special characteristics of the epoch photometry, with errors much larger in one direction than in another (Lindgren & Bastian 2022). The combined astrometry will also be useful, with significantly improved parallaxes and (especially) proper motions. We caution, however, against rushing to publish parameters for massive binaries from *Gaia* DR4 data for two reasons: the need to evaluate the precision and accuracy of the astrometry against calibrators (Maíz Apellániz et al. 2021c; Maíz Apellániz 2022) and the likely possibility that the originally derived parallaxes and (to a lesser degree) proper motions will be affected by the orbital motion of the system. When finding a solution in a many-dimensional space, one is likely to find local minima that are not the desired one and, in such cases, using external information (e.g. orbital periods or eccentricities) can significantly improve the solution, hence the usefulness of having previous spectroscopic orbits available. Astrometry will not be the only *Gaia* data that we will use, as DR4 will also include RVS time series for all sources brighter than $G_{RVS} = 14$ mag that will complement LiLiMaRlin, low-resolution epoch spectrophotometry, and epoch photometry (see next).

Epoch photometry. To model the eclipsing binaries and ellipsoidal variables (Martín-Ravelo et al. 2024 and MONOS III), M³W will also use epoch photometry from different sources. *TESS* (Ricker et al. 2015) will be the most useful, given its all-sky coverage, dynamic range, and high cadence, but its poor spatial resolution, low-frequency photometric calibration issues, and uneven long-term coverage require complementary data. On the one hand, *Gaia* DR4 will be even more useful than DR3 to study eclipsing binaries (Mowlavi et al. 2023), with a more uniform long-term coverage and better spatial resolution and photometric stability than *TESS* (at the cost of worse cadences). On the other hand, MUDEHaR (Holgado et al. 2024) will complement *Gaia* epoch photometry, targeting areas rich in massive stars to increase the time baseline and include H α variability.

High-resolution imaging and interferometry. Finally, for some systems we will complement all of the above information with lucky imaging and interferometry (Maíz Apellániz 2010; Sánchez-Bermúdez et al. 2013). The first is useful to determine or constrain long orbits with separations of 0'.1-1''.0 and the second for shorter orbits, in some cases by itself and in others in concert with high-resolution spectroscopy. We will also use the information available in the Washington Double Star catalog (WDS, Mason et al. 2001).

3. UNWIND

3.1. Package description

Within OWN, MONOS, and other multiplicity projects we have developed several codes related to orbit fitting written in IDL. The main novelty of the software package developed for the project is the UNWIND² disentangling code, which will be used within M³W for the main purpose of separating two or more components in a spectroscopic binary but also for other tasks such as the fitting and subtraction of the ISM component and the generation of high S/N spectra of SB1 systems (e.g. OWN I).

In addition to UNWIND, the package includes routines for single- and multi-component line fitting, cross correlation, and spectroscopic and visual orbit fitting, among others. Some of those will be used in this paper. Depending on the circumstances, the function fitting routines use (a) the non-linear least squares package MPFIT (Markwardt 2009) or (b) an analysis of the full relevant parameter space in the style of CHORIZOS for photometry (Maíz Apellániz 2004). As the number of dimensions can make the latter too computationally expensive, a search through the parameter space has to be performed in the case of visual orbits to look for different local minima (Maíz Apellániz et al. 2017; Maíz Apellániz 2019). For spectroscopic orbits we use MPFIT instead but we add a search with different seeds around the primary solution to check for the existence of alternative solutions. The long-term idea is to make UNWIND public.

3.2. UNWIND preprocessing and modules

Here we describe the data flow through the different modules (each with a different task) that make up UNWIND. In the next subsection we describe some of the issues that can be addressed with UNWIND.

As a preliminary step, all spectra have to be preprocessed using the LiLiMaRlin procedures for header and data uniformisation for different spectrographs, pre-rectification (to be revised

¹ As an example, the SB2 nature of the main target in this paper, GLS 11 448, was discovered in an $R \sim 2500$ spectrum from CAHA3.5.

² To be pronounced as / Δ n'w Δ ind/, not as / Δ n'wind/, as the purpose of the code is not to eliminate the effect of fast-flowing particles emitted from a star in its spectrum.

later, see below), and telluric-absorption calculation. The latter is done applying the telluric model of Gardini et al. (2013) with an extension into the near infrared that was added when CARMENES data were included in LiLiMaRlin. Alternatives telluric corrections can be used instead. By default, UNWIND requires that both the telluric-absorption corrected spectrum and the correction itself be passed along to the code in order to compute the weights used to combine spectra. However, it is possible to deactivate the requirement and to not apply telluric weights, for example for blue-violet spectra.

UNWIND itself uses the following modules in sequence:

Data reading, resampling, and rectification. The spectra are first read and resampled into a spectral grid with equal spacing in $\Delta\lambda/\lambda$ (logarithmic binning) to simplify velocity calculations. Rectification is done using wavelength points provided by the user after a careful examination of the spectra. This is done because of the high sensitivity of disentangling to rectification: it may be time consuming but it reduces systematic errors.

Telluric emission, standard ISM, and DIB fitting. A median spectrum from all epochs is used to eliminate the non-stellar contributions to the spectra. Telluric emission lines (and possibly residuals from broad telluric O₂ absorption lines) are removed by fitting (narrow) Gaussian profiles. The standard ISM (ionic and molecular) lines in absorption and emission are then directly subtracted but not fitted, as their profiles are usually non-Gaussian. In a future version we will implement the possibility of the subtraction of ISM emission lines such as H α or [O III] λ 5007 being refined on an epoch-by-epoch basis, as different spectrograph apertures and seeing conditions provide different degrees of contamination. Finally, DIBs are fitted with Gaussian profiles, as described below and in Appendix B. The default use is to fit only the overall velocity of the DIBs and the EW of each one, leaving the central wavelengths and FWHM fixed, but it is possible to fit more parameters. The UNWIND result on the median spectrum can be analysed at this point with an interactive spectrum viewer to fine-tune the rectification points and the fitted ISM (standard or DIBs) lines.

Spectral Energy Distribution, flux fraction, and velocity guesses. The code then reads the input guesses for the disentangling process. The (rectified) SED guesses can be derived from the data or from an input SED. In the current version, UNWIND includes a library of TLUSTY SEDs available from Lanz & Hubeny (2003, 2007) but users can include their own preferred SEDs. Flux fraction and velocity guesses are also provided by the user, the latter either as an orbital solution or as epoch velocities³. Note that those are not fitted by UNWIND itself but require an outer iteration (see next subsection). Also, in the current version flux fractions are constant for each component throughout all epochs but variable ones may be implemented in the future for eclipsing binaries.

Disentangling. UNWIND uses the standard disentangling technique of González & Levato (2006), see also Simon & Sturm (1994). The essence of the technique is that SED guesses are provided for each component, shifted in velocity for each epoch, and subtracted from the observed data. The residuals are then calculated and incorporated into new guesses, with the outcome iterated until convergence. As it is common in iterative fitting procedures, the result may alternate between two solutions in

consecutive iterations. For such a case, UNWIND offers the possibility of accelerating convergence by using the average of two iterations at a point in the process. It is possible in principle to include velocity changes into the next iteration but UNWIND leaves that to an outer iteration (see next subsection and examples in subsequent papers). The algorithm was originally designed to include only two components but with UNWIND it has been expanded into three or more. However, if an unconstrained component is added to the iterative procedure, the most likely outcomes are divergent non-physical solutions. For that reason, UNWIND allows only for fixed third lights, with the possibility of using the outer iteration to alternate among which components to fit, two at a time.

Output. During the disentangling process, the result of each iteration is displayed on the screen and, optionally, the final result is shown on an interactive spectrum viewer. In addition to the final result, the residuals for each epoch are also produced. An example of the final products for a spectroscopic GLS 11 448 Aa,Ab epoch (from the analysis in the next section) is shown in Fig. 1.

3.3. Disentangling issues

A typical use of UNWIND is iterative. For example, a combination of guesses for the orbit and flux fractions of the components may be tried, the output analysed, and a new orbit and/or flux fractions calculated. Under that scenario, the new orbit can be calculated by cross-correlating the UNWIND output with the epoch data (for simple SB1 systems) or by profile-fitting the epoch data with the UNWIND output (when two or more lights are present) and the new flux fractions obtained by comparing with single-star spectra or model SEDs⁴. Those new values may then be used for a new UNWIND run. Therefore, one can consider the process as containing an inner loop (the disentangling itself) and an outer loop over the orbital parameters and flux fractions. A simple case, such as one with two components with large velocity amplitudes and similar fluxes may require relatively little work but more complicated ones may require more effort and it is possible that the available epochs may not be enough to reach a satisfactory solution.

At this point we have tested UNWIND under quite different situations and in this subsection we discuss some of the issues that can complicate the disentangling of spectroscopic binaries. This should be taken as an introduction to such issues, as real examples provide a better guide to the process and its limitations. One such example, GLS 11 448, is analysed in the Sect. 4 and future papers of the series will study others. Of course, there are other issues that can lead to disentangling problems besides the ones mentioned here. Two obvious ones are the lack of adequate orbital phase coverage for the system and the addition of variability to one of both stars in the form of pulsations, winds, or disks. Another, perhaps less obvious one, is the need for an adequate rectification of the spectra, already mentioned above.

ISM subtraction. The ISM signature during the disentangling process could be approximated as a third light with fixed velocity and intensity⁵. However, as noted above, an unconstrained disen-

³ The current version of the code assumes that the two stars are not too different in T_{eff} , so that the flux fraction does not change much over the wavelength range of interest. For systems composed of e.g. a blue and a red star, a solution is to divide the disentangling process in several wavelength ranges and apply different flux fractions in each.

⁴ Using the wrong flux fractions for a system leads to components with too strong or too weak lines but, otherwise, has only a small influence in the disentangling process itself through the initial guesses. Hence, it is something that can be adjusted at the end of the process.

⁵ This would be an approximation, not an exact fit, for two reasons: [a] the variability of the ISM among epochs due to (rare) intrinsic changes or (common) aperture/seeing changes for emission lines and

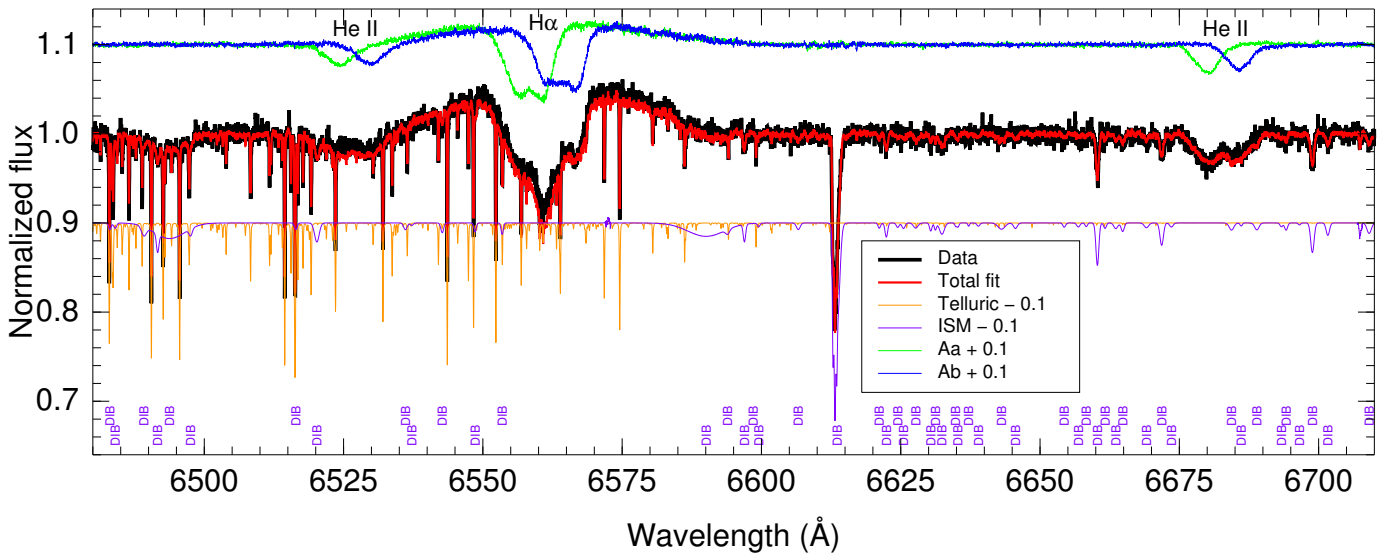


Fig. 1. Example of UNWIND output for the H α region of a GLS 11 448 Aa,Ab spectroscopic epoch and the result of combining 77 epochs. The top spectra (green and blue) show the normalized output for the two components, shifted horizontally to the velocities of the epoch and upwards 0.1 continuum units, and diluted by their flux fractions. The bottom (orange and purple) spectra show the fitted telluric lines, specific to this epoch, and ISM spectrum, mostly DIBs and common to all epochs, in the two cases shifted downwards 0.1 units. The central spectra show the data (black) and fit (red) for this epoch, the fit being the sum of the green and blue spectra (minus one to leave the continuum fixed) multiplied by the orange and purple spectra.

tangling process usually diverges from the physical solution. For those reasons, UNWIND calculates the ISM signature as a preliminary step and subtracts it from the observed spectra. Doing that is already a considerable task already for the standard (ionic or molecular) ISM lines as it requires compiling a library of the existing lines. For the case of GLS 11 448 below we detected almost 200 such lines of He I, Li I, Na I, Ca I, Ca II, K I, Rb I, C₂, CH, CH⁺, and CN. The problem becomes more important for DIBs, as they are more common, have broader profiles (in some cases similar to those of OB stellar lines), and can dominate the observed spectra of OB stars in some wavelength regions. That is one of the reasons why some previous disentangling efforts have been restricted to small wavelength regions instead of to the full spectral region observed. As obtaining such a broad wavelength range is one of the goals of UNWIND, we determined the most complete DIB library ever built, with a total of 631 in the 4000–17 100 Å range (Appendix B), and incorporated its subtraction into UNWIND. In Sect. 4 we show the result of the process for GLS 11 448, the first time an OB-type SB2 system has been disentangled over the entire 3820–11 000 Å range. The extracted DIB spectrum is of astrophysical interest by itself but we defer its study to a paper of the CollDIBs series (Maíz Apellániz 2015; Maíz Apellániz et al. 2019a).

Telluric-line subtraction. A similar issue is the elimination of telluric lines in disentangled spectra. This is a minor or non-existent problem at short wavelengths but becomes more important at longer ones, where it is compounded with the DIB subtraction issue mentioned above. An accurate telluric subtraction requires not only a good atmospheric model but also a spectrograph with good stability and a pipeline that delivers an accurate calibration. Among the spectrographs used in LiLiMaRlin, CARMENES (Quirrenbach et al. 2014; Caballero et al. 2025) excels in those two aspects and thanks to its data we have been able to disentangle some He II lines in the spectra of GLS 11 448

that are located in regions of high telluric contamination (see Sect. 4). In addition, the stability of CARMENES has allowed us to apply UNWIND to extract the spectra of some fullerene DIBs (see Appendix B) in regions with high telluric contamination by making the Earth play the role of a spectroscopic binary: the telluric lines move back and forth along with our orbital motion around the Sun while the DIBs remain fixed in velocity.

Third (and additional) lights. Given the high-order multiplicity typical of OB-type systems (MONOS I), it is common to find systems where three or more stars contribute to the observed spectra. In those cases, UNWIND requires that the flux(es) of the third (or higher) light(s) is/are fixed to an initial guess (but allowed to move by an orbital motion) and then an outer iteration is applied to the process, fixing one of the initial two stars and letting the other and the third one vary in a new UNWIND run. The process may be repeated as needed until convergence. An example of this UNWIND application is shown for BD −13 4929 in MONOS III. The system consists of two early B stars in a 2.9302 d orbit, each contributing 18% of the total light, in a long orbit around an O star that contributes the remaining 64% (and, which, for the purposes of UNWIND can be considered as stationary). The UNWIND result in Fig. A.6 of MONOS III shows a clear separation among the three components. For some stars in OWN I (τ CMa Aa,Ab, HD 101 190 Aa,Ab, HD 101 205 A,B, and HD 152 723 Aa,Ab) we also applied third-light analyses with UNWIND, some of which will be presented in more detail in future papers of this series.

Initial guesses. Any non-linear fitting process can be affected by the choice of initial guesses due to the possible existence of multiple local minima in the parameter space and this is especially so for a many-dimensional iterative process such as disentangling. This issue did not receive much attention when disentangling techniques were first applied (González & Levato 2006) but subsequent analyses (Quintero et al. 2020; Rosu et al. 2023) showed that a wrong choice of initial guesses can introduce spurious structures such as “horns” (emission peaks on both sides)

[b] the fact that the ISM imprint is a multiplicative signature in the sum of the observed fluxes.

Table 1. Spectrograph configurations used for GLS 11 448.

Code	Telescope	Spectrograph	Resolution	Wav. range (Å)
HET-B	HET	HRS	30 000	3820-4705
			30 000	4765-5725
HET-R	HET	HRS	30 000	5320-6250
			30 000	6395-7320
CAR	CAHA3.5	CARMENES	95 000	5240-9850
			80 000	9610-17 100
HAR-N	TNG	HARPS-N	115 000	3875-6905
FIES	NOT	FIES	25 000	3700-9000
CAFÉ	CAHA2.2	CAFÉ	95 000	3925-9225
Merc	Mercator	HERMES	85 000	3785-8995

around absorption lines. As in UNWIND it is possible to use different initial guesses, in subsequent papers we will explore the dependency of the final outcome on them.

Search for hidden components. A currently hot topic is the search for the signature of a companion in SB1 systems in order to detect whether it is a lower-mass normal star or a compact object (Shenar et al. 2020, 2022a,b, MONOS II, Mahy et al. 2022). In OWN I we already used UNWIND for this task and we note one aspect of the code that makes it especially well suited for it: Using the full spectral window for a given spectrograph gives us more chances to discover the hypothetical signature of the lower-mass companion. We will also explore this in future papers of the series.

4. Sample application: GLS 11 448 (= LS III +46 11)

Maíz Apellániz et al. (2015a) analysed GLS 11 448 using multi-epoch spectroscopy and discovered it is a near-twin, eccentric, very massive system with minimum masses of 38.8 M_⊙ and 35.6 M_⊙, respectively. In a follow-up paper, Maíz Apellániz et al. (2015b) analysed the foreground ISM affecting both GLS 11 448 and the nearby GLS 11 449 (= LS III +46 12), and detected two distinct kinematic components for both stars, indicating the presence of two clouds at different velocities. Despite their proximity in the plane of the sky, GLS 11 448 is significantly more extinguished than GLS 11 449 and different ISM indicators led Maíz Apellániz et al. (2015b) to suggest that the sightline of the former goes through the UV-shielded core of the progenitor cloud (ζ sightline, see Appendix B) while the sightline of the latter goes through less UV-shielded regions (σ sightline, see Appendix B). Within the Villafranca project (Maíz Apellániz et al. 2020) that is analysing Galactic stellar clusters with massive stars, Maíz Apellániz et al. (2022) used *Gaia* DR3 data to measure a distance of 2741⁺⁸⁶₋₈₁ pc to Berkeley 90, the cluster where both stars reside, which is consistent with the spectrophotometric distance to GLS 11 448 previously determined by Maíz Apellániz et al. (2015a).

In this section we use UNWIND to [a] derive a new SB2 orbit for GLS 11 448, [b] disentangle the two components (Aa and Ab) in the 3820-11 000 Å range, [c] determine new spectral classifications and stellar parameters, and [d] analyse the signature of the ISM in the disentangled spectra. In principle, this could be done by first using a small wavelength range with one or several prominent lines to derive the new orbit using as a seed the old one, applying the new orbit to the whole wavelength range to obtain the disentangled Aa and Ab plus the ISM spectra, and then proceeding to [c] and [d] above. However, that leaves us with the issue of partially undetermined systemic velocities, γ_{Aa}

and γ_{Ab} , because for O stars in general (and even more so for early-type supergiants such as GLS 11 448) wind infilling shifts the centroid of absorption lines, thus altering their values in different ways for different lines. This is a general problem for O stars that is especially relevant to the derivation of the peculiar velocities of runaway stars and will be treated in detail in a future paper of the M³W series. For GLS 11 448 we address it adding an outer iteration to the procedure above. First, we calculate the orbit (with approximate systemic velocities), disentangle the spectra according to it, and fit FASTWIND models to each of the two components. Those preliminary FASTWIND models are used to (a) check the flux fractions and (b) calculate the velocity shifts for H I, He I, and He II lines; select those lines with a good S/N in the spectra and small enough shifts; and use the difference between the disentangled spectra and the FASTWIND predictions to recompute new values of γ_{Aa} and γ_{Ab} to obtain the final orbit (using the dispersions as uncertainties). The final disentangled spectra can be calculated by running UNWIND one last time for the whole spectrum with the new orbit (if the flux fractions have changed) or simply by shifting in velocity the original UNWIND output (if they have not).

We use spectra from six spectrograph+telescope combinations, listed in Table 1. Four of the spectrographs (HARPS-N@TNG, FIES@NOT, CAFÉ@CAHA2.2, and HERMES@Mercator) have a single arm and the other two (HRS@HET and CARMENES@CAHA3.5) two simultaneous arms. CARMENES has a fixed configuration that yields a large coverage between 5240 Å and 17 100 Å (with some gaps) between the two arms. HRS@HET covers a smaller wavelength range and can be set up in either a blue (HET-B) or a red (HET-R) configuration, but it has the advantage of the much larger effective aperture of the telescope (9.2 m at the times the data were obtained). We used a total of 80 epochs, listed in Table 2. We note that different wavelengths were observed on a different number of epochs due to the coverage of each spectrograph and to the fact that the high extinction experienced by GLS 11 448 yields a poor S/N in the blue-violet region for small-aperture telescopes.

4.1. The new orbit

4.1.1. The orbital parameters

As explained above, our approach is to determine an initial orbit with UNWIND without paying attention to the systemic velocities (as those only shift the disentangled spectra in wavelength), obtain the stellar parameters from the result in subsection 4.2, and run UNWIND again applying the new γ values determined from them in order to obtain a self-consistent result. For the initial UNWIND run we start from the Maíz Apellániz et al. (2015a) orbit, disentangle the spectra, and use the results to fit the velocities to each epoch in the original data as a composite of the two components, Aa and Ab. We do this in four wavelength ranges: 4305-4705 Å (blue), 5390-5430 Å (He II λ 5411.53), 6505-6705 Å (red), and 8208-8267 Å (He II λ 8236.79). Each one of them has advantages and disadvantages, such as the larger number of lines in the blue range and the increasing S/N for the longer-wavelength regions. As it turns out, the solutions for the four wavelength ranges yield parameters that are consistent within two sigmas, so we selected the He II λ 5411.53 range as our primary source for three reasons: it has one of the strongest isolated lines in the whole optical spectrum, the S/N of the data there is considerably better than in the

Table 2. Spectroscopic epochs for GLS 11 448, see Table 1 for the code meanings.

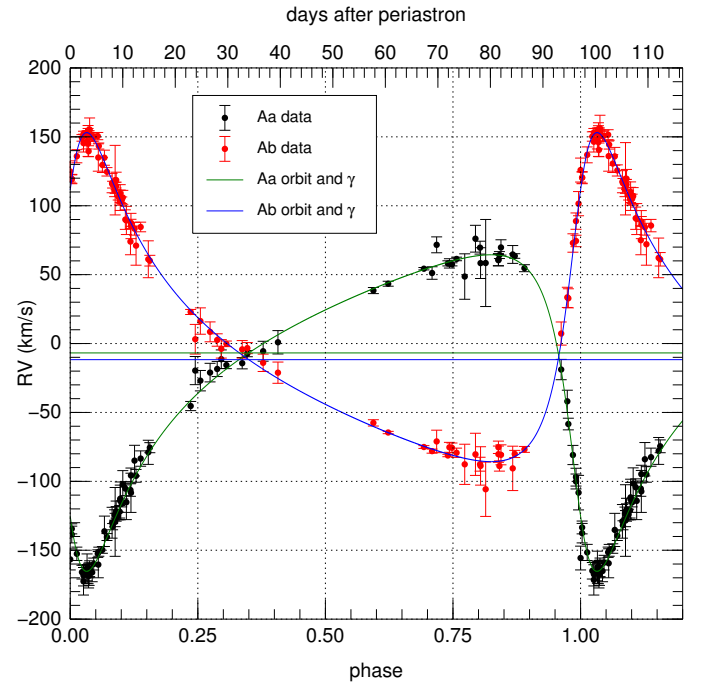
Code	Ev. date (YYYYMMDD)	BRJD (d)	Code	Ev. date (YYYYMMDD)	BRJD (d)	Code	Ev. date (YYYYMMDD)	BRJD (d)	Code	Ev. date (YYYYMMDD)	BRJD (d)
HET-B	20110621	55 734.77	HET-R	20121002	56 203.71	CAFÉ	20150818	57 253.56	CAR	20210720	59 416.52
HET-R	20110626	55 739.78	HET-R	20121004	56 205.73	CAFÉ	20150828	57 263.56	CAR	20210918	59 476.47
HET-R	20110913	55 818.79	HET-R	20121005	56 206.73	CAFÉ	20150831	57 266.51	FIES	20211020	59 508.37
FIES	20110915	55 820.49	CAFÉ	20121022	56 223.34	CAFÉ	20160327	57 475.70	CAR	20211023	59 511.39
FIES	20110917	55 822.36	HET-R	20121204	56 266.55	Merc	20160926	57 658.42	CAR	20220519	59 719.54
HET-B	20110928	55 833.75	CAFÉ	20121205	56 267.38	Merc	20160927	57 659.38	FIES	20220809	59 801.63
HET-R	20111002	55 837.72	HET-R	20121207	56 269.53	FIES	20171001	58 028.43	FIES	20221106	59 890.42
HET-R	20111003	55 838.72	CAFÉ	20121230	56 292.28	Merc	20171019	58 046.41	CAR	20221106	59 890.40
HET-R	20111006	55 841.71	CAFÉ	20130930	56 566.34	Merc	20171020	58 047.52	FIES	20221107	59 891.30
HET-R	20111007	55 842.71	Merc	20131028	56 594.33	Merc	20171025	58 052.38	FIES	20221108	59 892.35
HET-R	20111010	55 845.72	CAFÉ	20140413	56 761.62	Merc	20171026	58 053.35	FIES	20221109	59 893.45
HET-R	20111031	55 866.65	CAFÉ	20140414	56 762.61	Merc	20181018	58 410.48	FIES	20221111	59 895.34
HET-R	20111115	55 881.60	CAFÉ	20140805	56 875.51	Merc	20181025	58 417.39	CAR	20231211	60 290.32
HET-R	20111127	55 893.59	CAFÉ	20140806	56 876.37	CAR	20190824	58 720.40	HAR-N	20240720	60 512.65
HET-R	20120411	56 029.95	CAFÉ	20140807	56 877.45	FIES	20190831	58 727.59	Merc	20251013	60 962.39
HET-R	20120515	56 063.88	CAFÉ	20140814	56 884.38	FIES	20190901	58 728.55	Merc	20251018	60 967.44
HET-R	20120528	56 076.82	CAFÉ	20140816	56 886.53	FIES	20190902	58 729.49	Merc	20251019	60 968.38
HET-R	20120610	56 089.82	CAFÉ	20140818	56 888.54	Merc	20200613	59 014.66	Merc	20251020	60 969.49
HET-B	20120827	56 167.81	Merc	20150529	57 172.72	Merc	20200629	59 030.70	Merc	20251021	60 970.41
CAFÉ	20120907	56 178.54	Merc	20150531	57 174.72	CAR	20210622	59 388.62	Merc	20251022	60 971.49

Table 3. GLS 11 448 orbit results.

Quantity	Units		
T_0	BRJD	56 003.299 ±0.092	
P	d	97.1696±0.0023	
e		0.5831±0.0030	
ω	degrees	130.67 ±0.52	
$(M_{Aa} + M_{Ab}) \sin^3 i$	M_\odot	69.37 ±0.55	
q		0.9622±0.0051	
$(a_{Aa} + a_{Ab}) \sin i$	au	1.6997±0.0045	
		Aa	Ab
K	km/s	114.86 ±0.56	119.38 ±0.45
γ	km/s	-6.8 ±4.7	-11.7 ±3.4
$M \sin^3 i$	M_\odot	35.36 ±0.49	34.01 ±0.51
$a \sin i$	au	0.8334±0.0035	0.8662±0.0029

blue, and its central location in the spectrum allows us to use the largest number of epochs of any range.

The orbital parameters (including the systemic velocities resulting from the outer iteration derived in the next subsection) are listed in Table 3 and the orbit is plotted in Fig. 2. Not including the γ values, the parameters are very similar to those of Maíz Apellániz et al. (2015a), in most cases within two sigmas. The velocity amplitudes are slightly lower, leading to lower minimum (Keplerian) masses, and the mass ratio is now even closer to 1.0 than before. The masses are analysed in Sect. 4.2 in conjunction with the values determined from the disentangled spectra. The most significant change for the parameters is the reduction of the uncertainties, with the one for the period now an order of magnitude lower. This is an expected effect of adding epochs with better measurements and, for the period, of extending the time coverage.


Fig. 2. Phased radial velocity curves for GLS 11 448 Aa and Ab.

4.1.2. The systemic velocities

In Sect. 4.2 we fit FASTWIND models to the disentangled spectra to derive synthetic H+He spectra for GLS 11 448 Aa and Ab that include the effect of unresolved multiplets and lines from different species and of infilling from stellar winds. Here we use them to adjust the systemic velocities, for which we analyse the different choices:

H I. Hydrogen lines are intrinsically broader than He lines; they include contributions from partially unresolved He II lines, which are especially important for stars of very early subtypes

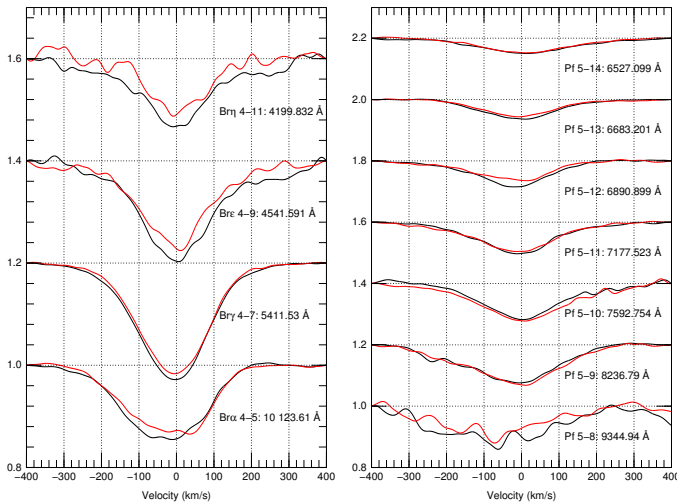


Fig. 3. Disentangled Brackett (left) and Pfund (right) He II series of GLS 11 448 Aa (black) and Ab (red). The spectra are normalised, displaced in continuum units, and placed in the rest velocity frame of each component systemic velocity without taking into account wind infilling effects (hence, the small displacement in centroids towards the blue). Differences in S/N are caused by extinction increasing towards the blue and by the residuals of telluric-line subtraction (the most obvious ones being for Pf 5-8 and 5-10). The even-numbered Brackett series is not shown because of the proximity of the H I Balmer series. The spectra have been degraded to $R = 10\,000$ for display purposes.

such as GLS 11 448; and some (especially H α) are strongly affected by wind infilling. For H α , the inclusion of the He II component in the FASTWIND models leads to a displacement towards the blue of 8-15 km/s depending on the method used to determine the central value of such an asymmetric profile⁶. The inclusion of wind infilling leads to an even more complicated effect in H α , with an absorption in the core and emission in the wings (Fig. 1), with the absorption core being displaced towards the blue by an additional 25-80 km/s (with the exact values depending again on the method used to determine them). However, even for a line less affected by wind infilling such as H β , the effect is ~ 15 km/s for GLS 11 448 Aa and Ab. For those reasons, we did not use H I lines to determine the systemic velocities.

He I. Neutral helium lines have the advantage of being intrinsically narrower than either H I or He II lines, which would make them better candidates for measuring the systemic velocities, but for GLS 11 448 they have the disadvantage of their weakness. Indeed, only three He I lines are detected in our data in the 3820-11 000 Å range ($\lambda 4471.55$, $\lambda 5875.70$, and $\lambda 7065.3$, all weak) and, furthermore, all are multiplets. Hence, we decided against using He I lines to determine the systemic velocities.

He II. Ionised helium lines⁷ have an intrinsic width that is intermediate between those of H I and He I lines but for GLS 11 448 they have two important advantages: they are singlets (other than for small fine-structure splittings) and they are very strong. For those reasons, we selected the best five He II lines in terms of strength, isolation, and absence of telluric contamination ($\lambda 4199.832$, $\lambda 4541.591$, $\lambda 5411.531$, $\lambda 7177.523$,

⁶ In addition to the effect of the two species, each line is itself a multiplet with a small velocity spacing due to fine structure that is usually erased by the effects of rotation and turbulence.

⁷ For He II we use the Atomic Line List v.2.04, <https://line-list.pa.uky.edu/atomic/>, for the central wavelengths.

and $\lambda 8236.79$, Fig. 3) and averaged their results for our primary determination of the systemic velocities. We exclude the He II $\lambda 4685.71$ Paschen line because it is strongly affected by winds, which was the reason for Walborn (1971) using it as the primary luminosity criterion for stars earlier than O9 (see subsection 4.2 for its effect on spectral classification).

Metallic lines. There is an O III line ($\lambda 592.252$), two N IV lines ($\lambda 5200.41$ and $\lambda 6380.7$), and two N V lines ($\lambda 4603.74$ and $\lambda 4619.97$), all in absorption, that, though weak, can be used to determine the systemic velocities, as they are even intrinsically narrower than He I lines. However, our current FASTWIND models do not include them, so we cannot calculate their wind infilling. However, we retain them to compute their averages as an alternative determination of the systemic velocities.

Our results for the systemic velocities based on the five He II lines are given in Table 3. They agree within one sigma for the two components, a good sign of the absence of systematic effects. The correction of the wind infilling is significant, between 7 km/s and 11 km/s depending on the line, in all cases in the sense of the wind moving the centroid of the line towards the blue. The alternative values derived from the five metallic lines are -7.2 ± 3.1 km/s for Aa and -11.5 ± 6.3 km/s for Ab. Those are consistent with the ones from He I, with the scatter likely arising from the weakness of the lines and the uncorrected effect of wind infilling affecting them to different degrees. This issue could be verified in the future with an atmospheric modelling of those metallic lines. The γ values for both components are higher than the ones from Maíz Apellániz et al. (2015a) by about ~ 10 km/s, which is consistent with the previous paper not taking into account wind infilling effects. As we will see in future papers of the series, such systematic effects are commonly lurking among published radial velocity results for O stars in the literature.

4.1.3. On the existence of an apsidal motion

Given the high eccentricity of the GLS 11 448 Aa,Ab orbit and our 14-year spectroscopic coverage, we investigate whether our data are good enough to determine a possible apsidal motion ($d\omega/dt$) in the system. For the three wavelength ranges for which we have the best coverage (blue, He II $\lambda 5411.53$, and red) we fitted orbits leaving $d\omega/dt$ as a free parameter (Rosu et al. 2020a). In the three cases we obtained very low values, with the highest one being 0.22 ± 0.13 degrees/a, which corresponds to 3.0 ± 1.8 degrees in 14 years, so our results are consistent with a non-detection of apsidal motion. How does this compare with what we expect from theory? For the general relativistic effect, assuming two $75 M_{\odot}$ stars (see subsection 4.2), the predicted result (Rosu 2025) is 0.004 degrees/a, which is more than one order of magnitude smaller than the uncertainty in the measurement above. For the Newtonian effect caused by tides and rotation, the exact value depends on the k_2 internal stellar structure constant, for which there is a possible range of values, but the final result is a few times lower (0.0005 to 0.002 degrees/a) than the general relativistic effect. Therefore, we conclude that our non-detection of an apsidal motion is consistent with theory and that GLS 11 448 is a system where apsidal motion should be very hard to detect, as even a century of data would yield a total apsidal motion of a fraction of a degree after almost 400 orbits.

4.2. The disentangled spectra

After deriving the new orbital solution in the previous subsection, we used it to disentangle the full 3820-11 000 Å range.

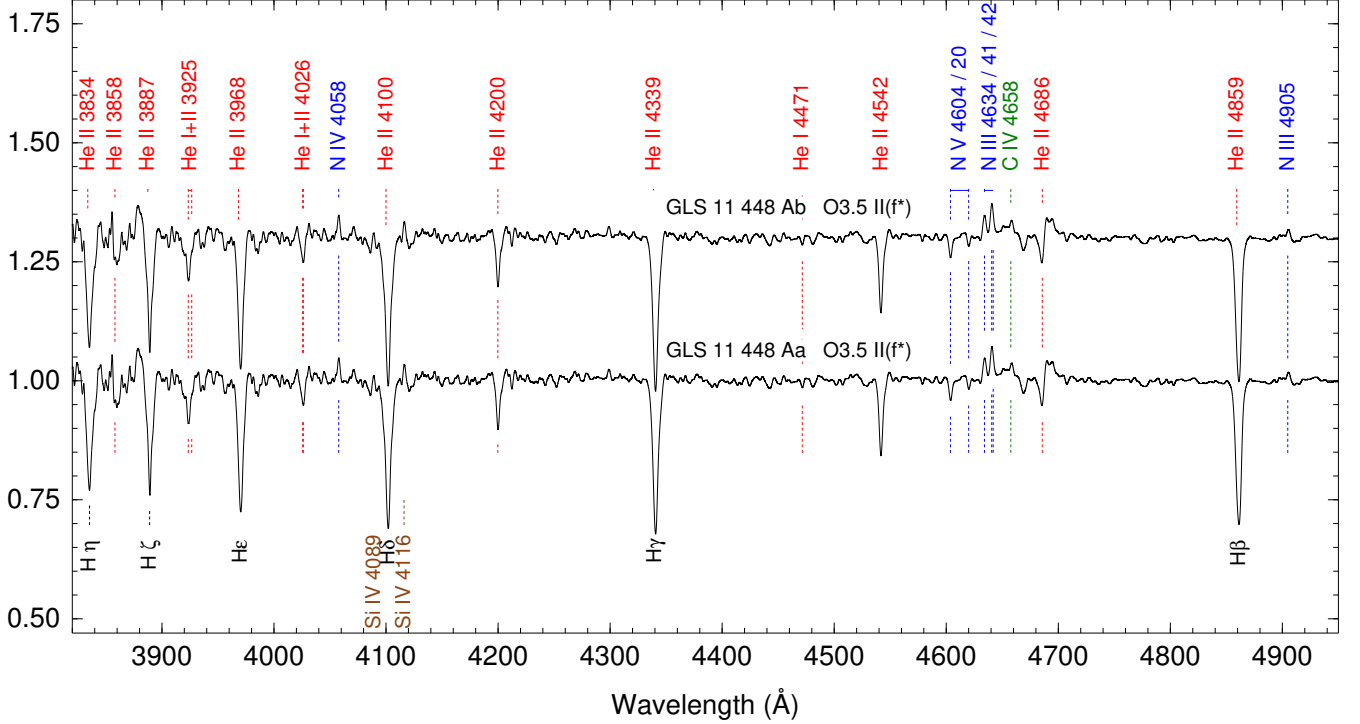


Fig. 4. Disentangled blue-violet spectra of GLS 11 448 Aa,Ab shifted to the stellar reference frame and degraded to the spectral classification resolution $R = 2500$. The two spectra are almost identical and there is no sign of the subtracted ISM. This is an update of Fig. 2 in Maíz Apellániz et al. (2015a), where the S/N is higher but the spectra are not disentangled and the ISM is not subtracted.

To our knowledge, this is the first time an O-type SB2 system has been disentangled in such a large wavelength range, including regions of significant telluric absorption and hundreds of DIBs. Such broad wavelength coverage allows for the analysis of a large number of lines of the same species (Fig. 3, which does not include several Paschen and Humphreys He II lines also detected). For similar efforts over a range about one half of that (but avoiding regions of strong telluric absorption), see e.g. Rosu et al. (2020a, 2022a).

As part of the outer iteration described above and, given the previous results of Maíz Apellániz et al. (2015a), we initially assumed a flux fraction for Aa of 0.50 (i.e. a flux ratio of 1:1 between the two components). Such an assumption leads to the two components having almost identical spectra (Figs. 3 and 4), with EWs that conform to what is expected from observed stars of similar spectral types and to FASTWIND models of those T_{eff} and luminosities (see below). Therefore, we left the value of the flux fractions as 0.50 and we estimate that the magnitude difference between the two components is at most 0.1 mag. This should be verified in the near future by resolving the system with interferometry, something that may be possible with CHARA given that the maximum separation in the eccentric orbit is expected to be around 1 mas.

The disentangled blue-violet spectra were degraded to $R = 2500$ for their spectral classification. Maíz Apellániz et al. (2015a) classified both components as O3.5 If*, with the spectral subtype derived from the ratios of nitrogen lines (Walborn et al. 2002) and the luminosity class derived from the He II $\lambda 4685.71$ line. At that time the spectral classification grid only had a II luminosity class down to O6 (Maíz Apellániz et al. 2016) but since then it has been extended to earlier O subtypes when He II $\lambda 4685.71$ has a P-Cygni profile, following the same cri-

Table 4. GLS 11 448 parameter results.

Quantity	Units	Aa	Ab
Spectral type		O3.5 II(f*)	O3.5 II(f*)
T_{eff}	kK	43.8 ± 3.0	45.3 ± 3.0
$\log g$	cgs	3.86 ± 0.27	3.93 ± 0.21
R	R_{\odot}	15.6 ± 0.8	15.6 ± 0.6
$\log(L/L_{\odot})$		5.91 ± 0.12	5.97 ± 0.11
$\log(Q/L_{\odot})$		4.09 ± 0.16	4.05 ± 0.12
$\log Q$	cgs	-12.33 ± 0.95	-12.31 ± 0.95
$v \sin i$	km/s	96.0 ± 9.6	87.0 ± 8.7
Θ_{RT}	km/s	64.0 ± 6.4	60.0 ± 6.0
M_{spec}	M_{\odot}	65.0 ± 36.0	77.0 ± 34.0
M_{evol}	M_{\odot}	70.0 ± 10.0	76.0 ± 11.0
age	Ma	1.59 ± 0.56	1.32 ± 0.56

terion as for mid-O subtypes (Maíz Apellániz et al. in prep.). As that is the case for both components of GLS 11 448, we change their spectral classification to O3.5 II(f*).

After spectral disentangling, the spectrum of each component was analysed independently following the methodology described in Holgado et al. (2025a). The effective temperature (T_{eff}) and surface gravity ($\log g$) were derived through quantitative spectroscopic analysis using a grid of FASTWIND stellar atmosphere models (Santolaya-Rey et al. 1997; Puls et al. 2005) and the IACOB-GBAT fitting tool (Simón-Díaz et al. 2011a), while projected rotational velocities ($v \sin i$) were determined with IACOB-BROAD following the Fourier-transform and goodness-of-fit approach described by Simón-Díaz & Herrero (2007, 2014). In both cases, the analysis was based on the N V $\lambda 4603.74$ line. We used the Berkeley 90 distance of Maíz Apellániz et al. (2022) and the extinction pa-

rameters of Maíz Apellániz & Barbá (2018). Stellar radii (R), luminosities (L), and spectroscopic luminosities ($\mathcal{L} = T_{\text{eff}}^4/g$, Langer & Kudritzki 2014; de Burgos et al. 2024) and masses (M_{spec}) were derived using standard relations involving the synthetic flux of the best-fitting FASTWIND model (Kudritzki 1980; Holgado 2019). The surface gravity was corrected for centrifugal acceleration following Herrero et al. (1992) and Repolust et al. (2004). Uncertainties in the final fundamental parameters were estimated through Monte Carlo propagation of the errors in the spectroscopic and photometric quantities. To calculate the evolutionary initial masses (M_{evol}) and ages, we used the 3-D grid of stellar models of Maíz Apellániz (2013) which for massive stars is based on the Geneva evolutionary tracks without rotation (Lejeune & Schaerer 2001). The masses were computed from the real luminosity instead of from the spectroscopic luminosity, as the distance and extinction are more precisely determined than the gravities, which is also the reason why the M_{spec} uncertainties are larger than those of M_{evol} . Our results include the effect of the correlated nature of the derived quantities and were compared with the Bonnsai tool (Schneider et al. 2016), which uses the alternative Bonn evolutionary tracks, with an agreement better than one sigma.

The parameters listed in Table 4 confirm the results of the spectral classification in the sense that the two components are very similar, to the point that all results are within half a sigma of either uncertainty. The T_{eff} uncertainties are relatively large because for very early spectral subtypes the He I lines used in our procedure become very weak (Walborn et al. 2002). In order to improve them a future analysis should use nitrogen lines instead.

The most important result is the extremely high evolutionary masses derived for both components of $70 \pm 10 M_{\odot}$ and $76 \pm 11 M_{\odot}$, respectively. They are the highest masses ever derived for any Galactic O star (excluding “early-slash” stars, see below). The closest contenders are Cyg OB2-9 A (Nazé et al. 2010), Cyg OB2-B17 A (Stroud et al. 2010), HD 93 129 Aa (Maíz Apellániz et al. 2017, an improved measurement will be the subject of an incoming M³W paper), and WR 21a B (Barbá et al. 2022), all of them with values 10-20 M_{\odot} lower than the ones for GLS 11 448 (in different degrees of certainty). Stars more massive than GLS 11 448 Aa,Ab are expected to be born with winds strong enough to appear of type WNh even in the ZAMS, with WR20a being a twin system of such stars with masses of $83 \pm 5 M_{\odot}$ and $82 \pm 5 M_{\odot}$, respectively (Bonanos et al. 2004). Similarly, GLS 22 159 A (= WR21a A), an “early-slash” or early Of/WN star (Sota et al. 2014) classified as O2 Ifc*/WN5 (OWN II) has a mass of $93.2^{+2.2}_{-1.9} M_{\odot}$ (Barbá et al. 2022). Therefore, if our results are confirmed, the limit between O and “early-slash”+ WNh stars appears to be around 80 M_{\odot} but it is possible that once rotation, metallicity, and evolutionary effects are included, an overlap in masses may reveal itself (for example, Cyg OB2-9 A and Cyg OB2-B17 A are more evolved than GLS 11 448 Aa,Ab and HD 93 129 Aa). The main obstacle to elucidate this topic is the rarity of these objects, which enhances the importance of our result. Given that our high masses are calculated from evolutionary tracks, they should be confirmed with a measurement of the $\sin i$ of the orbit from interferometry. To reconcile the values of the Keplerian minimum masses with the evolutionary masses the inclination should be around 50 degrees.

4.3. The foreground ISM

As described in Appendix B, we used GLS 11 448 as the primary standard to build the DIB library for UNWIND. Table B.2 list the characteristics of the 631 DIBs in the library, including

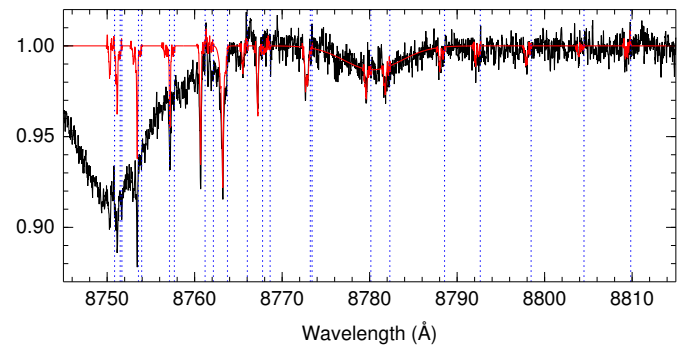


Fig. 5. Section of the UNWIND extraction for GLS 11 448 Aa (in the rest frame of the star determined from Table 3) with a significant portion of the Phillips C₂ (2,0) band. The black line is the star+ISM line (with the most prominent feature being the H I Pa α line) and the red line the fitted ISM, including the C₂ lines, DIBN8764, and DIBI8781. The vertical lines mark the expected position of the C₂ lines in the rest frame of the star, note the velocity displacement.

the EWs for GLS 11 448, and Table B.3 gives more details about the 37 for which we used multiple Gaussians. Those tables can be considered expanded versions of Table 2 in Maíz Apellániz et al. (2015b). In this subsection we use the UNWIND results to briefly expand the results from that paper.

Maíz Apellániz et al. (2015b) proposed that the reason why the GLS 11 448 sightline is more extinguished than that of GLS 11 449 but with lower EWs for most DIBs is that the additional extinction originates in a UV-shielded (ζ sightline) cloud core that contributes little to the DIB EWs. One consequence of that would be the presence of C₂ absorption on the GLS 11 448 sightline, something that is readily apparent in the UNWIND ISM output, where we detect strong signals in the Phillips (1,0), (2,0), and (3,0) bands around 10 150 Å, 8765 Å, and 7720 Å, respectively (Figs. 5 and B.1). We even detect the seldom seen Phillips (0,0) band around 12 100 Å (Hamano et al. 2019) in a range of our CARMENES spectra that we did not process with UNWIND, though for that band we lose some lines that fall in an order gap. The velocity of the C₂ lines indicates that it is associated with the cloud with the most negative velocity of the two along the sightline (Fig. B.1). On the other hand, we also analysed equivalent spectra (with shorter total exposure time and, hence, S/N) of GLS 11 449 that we also obtained with CARMENES and we were only able to detect a weak signal, with EWs roughly an order of magnitude lower than for GLS 11 448. Therefore, the existence of such a molecular-gas rich, UV-shielded core along the GLS 11 448 sightline (that has little or no effect on the GLS 11 449 sightline) is confirmed.

An aspect of the GLS 11 448 sightline that could not be studied by Maíz Apellániz et al. (2015b) is the presence of He I interstellar absorption. Under normal conditions in the ISM, most He I atoms in the ISM are in the singlet $1s^2 \ ^1S_0$ ground state, which requires EUV photons to excite and, for that reason, makes He I not detectable in absorption at longer wavelengths (the same reason why H I is not detected, either, even though in that case the required energies are lower). In an H II region, however, some recombinations take place through the triplet configuration and those end up in the metastable $1s2s \ ^3S_1$ level. There, they may stay long enough to absorb radiation from a background star and produce interstellar absorption lines (Draine 2026). Three such lines have wavelengths longer than 3000 Å:

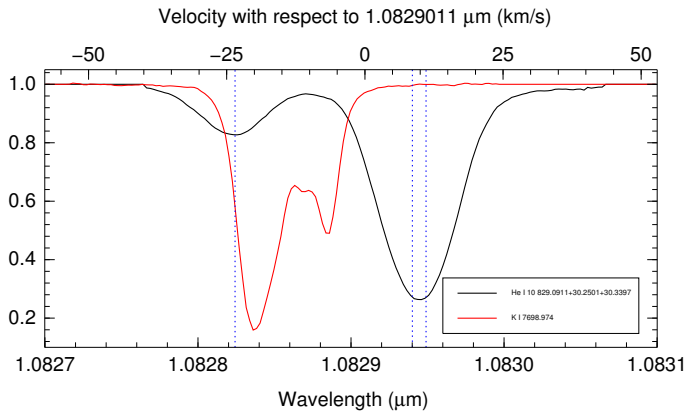


Fig. 6. A comparison of the profiles of the interstellar He I $\lambda 10 830$ triplet and K I $\lambda 7698.974$ line in the GLS 11 448 sightline, with the latter placed in the velocity reference frame of the first component of the He I triplet ($10 829.0911 \text{ \AA}$), see also Fig. B.1. The dashed blue vertical lines mark the tentative He I velocity of -23.5 km/s in our barycentric reference frame, which is blueshifted with respect to either K I cloud. Stellar lines are broader in velocity than the plotted range (see e.g. Fig. 3).

the hard-to access from the ground $\lambda 3187.7$ plus $\lambda 3888.6$ and $\lambda 10 830$. All three are triplets but the separation of the third one is considerable larger (1.25 \AA) than that of the other two (0.16 \AA for the second and even less for the first). $\lambda 3888.6$ was first detected in absorption in an O star immersed in an H II region by Wilson (1937). Some authors have attempted or suggested the detection of $\lambda 10 830$ in absorption in OB-star sightlines (Indriolo et al. 2009; Galazutdinov & Krelowski 2012) but, to our knowledge, without success.

In the UNWIND output we detect a clear He I $\lambda 3888.6$ interstellar absorption with an EW of $\sim 60 \text{ m\AA}$ but with a large uncertainty due to the low S/N in our data at short wavelengths. More importantly, we detect for the first time the $\lambda 10 830$ triplet in absorption in an OB-star (Fig. 6), with a very strong EW of 568 m\AA including the three components of the triplet. Both $\lambda 10 829.0911$ and the unresolved $\lambda \lambda 10 830.2501, 30.3397$ doublet are consistent with a (solar) barycentric velocity of -23.5 km/s , blueshifted with respect to the two components detected in the rest of the absorption lines (Fig. B.1). This could be caused by an expansion of the H II region or possibly by the complicated radiation transport involved (Draine 2026). The lack of stellar absorption in such an early O-spectrum makes the detection of the interstellar line easier but we note that the stellar component would be much broader (Fig. 3).

5. Summary and future work

In this first M³W paper we have established the objectives of the project, which revolve around the determination of the individual and collective multiplicity properties of the largest sample of massive stars in the solar neighbourhood ever assembled. The sample will be built from the ALS catalog and data will consist of a combination of spectroscopy, astrometry, and photometry obtained from the ground and from space. We have presented the software package that will be used for the analysis, with an emphasis on the UNWIND spectral disentangling tool. We have produced the most complete DIB library to date and for the massive near-twin binary GLS 11 448 we have (a) computed a new SB2 orbit, (b) determined that it is composed of the two non-

early-slash O stars with the highest evolutionary masses known, and (c) detected the He I $\lambda 10 830$ triplet in absorption in an OB-star for the first time ever.

M³W is a long-term project for which we have already planned or started writing several papers:

- A review of stellar multiplicity in the solar neighbourhood combining the results from OWN, MONOS, and the literature. Such a paper was the declared goal of OWN and MONOS and will be our starting point for further analyses.
- An analysis of the systemic velocities and variability of single O stars to better establish the detection limits of spectroscopic binaries and determine the systematic and random uncertainties in the systemic velocities caused by pulsations and line infilling.
- Several papers on specific systems for which we have determined new or updated old spectroscopic orbits. In particular, one will be devoted to the analysis of some OWN targets which will also be used to highlight some of the UNWIND capabilities.
- A paper on the complex hierarchical system $\tau \text{ CMa}$ (Rosu et al. 2025).
- The effect of the initial guesses on the final result of the disentangling process.
- Once *Gaia* DR4 epoch data becomes available, we expect to combine our existing spectroscopy with the new data to analyze the orbits of OB stars with compact companions.

Acknowledgements. J. M. A., S. R., E. M. F., and J. A. M. C acknowledge support from the Spanish Government Ministerio de Ciencia e Innovación and Agencia Estatal de Investigación (10.130 39/501 100 011 033) through grant PID2022-136640 NB-C22. R. C. G. acknowledges support in the form of travel funds from the Red Española de *Gaia*. G. H. and S. S.-D. and G.H. acknowledge support from the Spanish Government Ministerio de Ciencia e Innovación, Agencia Estatal de Investigación (10.130 39/501 100 011 033) and the European Regional Development Fund, FEDER under grants PID2021-122397 NB-C21 and PID2024-159329 NB-C21 S. R. acknowledges support from the Swiss National Foundation (SNF) project No 212 143. M. A.-M. acknowledges support from the “La Caixa” Foundation (ID 100010434) under the fellowship code LCF/BQ/PI23/11 970 035. This paper includes data obtained with: the 1.2 m Mercator Telescope (MT), the 2.6 m Nordic Optical Telescope (NOT), the 3.6 m Telescopio Nazionale Galileo (TNG), the 4.2 m William Herschel Telescope (WHT), the 10.4 m Gran Telescopio Canarias (GTC) at the Observatorio del Roque de los Muchachos, La Palma, Spain; the 2.2 m and 3.5 m Telescopes (CAHA2.2 and CAHA3.5) at the Centro Astronómico Hispano-Alemán/Andaluz, Almería, Spain; the 2.2 m Telescope (OLS2.2) and the 3.6 m Telescope (OLS3.6) at the Observatorio de La Silla, Chile; the 8.2 m Very Large Telescope (VLT) at Cerro Paranal, Chile; and the 9.2 m Hobby-Eberly Telescope (HET) at MacDonal Observatory, U.S.A. We thank the staff at those observatories for their support. The paper is dedicated to Rodolfo H. Barbá, who spent a considerable amount of time in laying the original work for this project but unfortunately passed away before seeing the fruits of his work in the form of this first paper of the series.

References

- Almeida, L. A., Sana, H., Taylor, W., et al. 2017, *A&A*, 598, A84
- Ansín, T., Gamen, R., Morrell, N. I., et al. 2023, *MNRAS*, 525, 4566
- Arias, J. I., Barbá, R. H., Gamen, R. C., et al. 2010, *ApJL*, 710, L30
- Banyard, G., Sana, H., Mahy, L., et al. 2022, *A&A*, 658, A69
- Barbá, R. H., Gamen, R. C., Arias, J. I., et al. 2010, in *RMxAC*, Vol. 38, 30–32
- Barbá, R. H., Sabín-Sanjulián, C., Arias, J. I., et al. 2020, *MNRAS*, 494, 3937
- Barbá, R. H. et al. 2017, in *IAU Symposium vol. 329*, 89–96
- Barbá, R. H. et al. 2022, *MNRAS*, 516, 1149
- Bernstein, L. S. et al. 2018, *ApJ*, 859, 174
- Bonanos, A. Z., Stanek, K. Z., Udalski, A., et al. 2004, *ApJL*, 611, L33
- Britavskiy, N., Mahy, L., Lennon, D. J., et al. 2025, *A&A*, 698, A40
- Caballero, J. A., Seifert, W., Quirrenbach, A., et al. 2025, arXiv:2503.05501
- Campbell, E. K., Holz, M., Gerlich, D., & Maier, J. P. 2015, *Nature*, 523, 322
- Campillay, A. R., Arias, J. I., Barbá, R. H., et al. 2019, *MNRAS*, 484, 2137
- Carretero-Castrillo, M., Ribó, M., & Paredes, J. M. 2023, *A&A*, 679, A109
- de Burgos, A. et al. 2024, *A&A*, 687, A228
- de Jong, R. S., Agertz, O., Berbel, A. A., et al. 2019, *The Messenger*, 175, 3
- Draine, B. T. 2026, *ApJ*, 999, 3
- Duke, D. 1951, *ApJ*, 113, 100
- Dunstall, P. R., Dufton, P. L., Sana, H., et al. 2015, *A&A*, 580, A93
- Fan, H., Hobbs, L. M., Dahlstrom, J. A., et al. 2019, *ApJ*, 878, 151
- Galazutdinov, G., Moutou, C., Musaev, F., & Krelowski, J. 2002, *A&A*, 384, 215
- Galazutdinov, G. A. & Krelowski, J. 2012, *MNRAS*, 422, 3457
- Gamen, R., Barbá, R. H., Walborn, N. R., et al. 2015a, *A&A*, 583, L4
- Gamen, R., Putkuri, C., Morrell, N. I., et al. 2015b, *A&A*, 584, A7
- Gamen, R. C., Gosset, E., Morrell, N. I., et al. 2006, *A&A*, 460, 777
- Gamen, R. C., Gosset, E., Morrell, N. I., et al. 2008, in *RMxAC*, Vol. 33, 91–93
- Gardini, A., Maíz Apellániz, J., et al. 2013, in *HSA 7*, 947–947
- González, J. F. & Levato, H. 2006, *A&A*, 448, 283
- Hamano, S., Kawakita, H., Kobayashi, N., et al. 2019, *ApJ*, 881, 143
- Hamano, S., Kobayashi, N., Kawakita, H., et al. 2022, *ApJS*, 262, 2
- Heger, M. L. 1922, *Lick Observatory Bulletin*, 10, 146
- Herrero, A. 2007, *Highlights of Astronomy*, 14, 201
- Herrero, A. et al. 1992, in *The Atmospheres of Early-Type Stars*, Vol. 401, 21
- Hobbs, L. M., York, D. G., Snow, T. P., et al. 2008, *ApJ*, 680, 1256
- Hobbs, L. M., York, D. G., Thorburn, J. A., et al. 2009, *ApJ*, 705, 32
- Holgado, G. 2019, PhD thesis, Instituto de Astrofísica de Canarias, Spain
- Holgado, G., Maíz Apellániz, J., et al. 2024, in *EAS2024*, 124
- Holgado, G., Simón-Díaz, S., Barbá, R. H., et al. 2018, *A&A*, 613, A65
- Holgado, G., Simón-Díaz, S., Haemmerlé, L., et al. 2020, *A&A*, 638, A157
- Holgado, G., Simón-Díaz, S., & Herrero, A. 2025a, *A&A*, 703, A175
- Holgado, G. et al. 2025b, *A&A*, 701, A246 (MONOS III)
- Indriolo, N., Hobbs, L. M., Hinkle, K. H., & McCall, B. J. 2009, *ApJ*, 703, 2131
- Jenniskens, P. & Desert, F.-X. 1994, *A&AS*, 106, 39
- Jin, S., Trager, S. C., Dalton, G. B., et al. 2024, *MNRAS*, 530, 2688
- Kobulnicky, H. A., Kiminki, D. C., Lundquist, M. J., et al. 2014, *ApJS*, 213, 34
- Krelowski, J., Schmidt, M., & Snow, T. P. 1997, *PASP*, 109, 1135
- Kudritzki, R.-P. 1980, *A&A*, 85, 174
- Langer, N. & Kudritzki, R. P. 2014, *A&A*, 564, A52
- Lanz, T. & Hubeny, I. 2003, *ApJS*, 146, 417
- Lanz, T. & Hubeny, I. 2007, *ApJS*, 169, 83
- Lejeune, T. & Schaerer, D. 2001, *A&A*, 366, 538
- Lindgren, L. & Bastian, U. 2022, *GAIA-C3-TN-LU-LL-061*
- Mahy, L., Lanthermann, C., Hutsemékers, D., et al. 2022, *A&A*, 657, A4
- Maíz Apellániz, J. 2004, *PASP*, 116, 859
- Maíz Apellániz, J. 2008, *ApJ*, 677, 1278
- Maíz Apellániz, J. 2010, *A&A*, 518, A1
- Maíz Apellániz, J. 2013, in *HSA VII*, 657–657
- Maíz Apellániz, J. 2015, *MmSAL*, 86, 553
- Maíz Apellániz, J. 2019, *A&A*, 630, A119
- Maíz Apellániz, J. 2022, *A&A*, 657, A130
- Maíz Apellániz, J. & Barbá, R. H. 2018, *A&A*, 613, A9
- Maíz Apellániz, J. & Barbá, R. H. 2020, *A&A*, 636, A28
- Maíz Apellániz, J. et al. 2004, *ApJS*, 151, 103
- Maíz Apellániz, J. et al. 2011, in *HSA 6*, 467–472
- Maíz Apellániz, J. et al. 2012, in *ASP Conference Series*, Vol. 465, 484
- Maíz Apellániz, J. et al. 2015a, *A&A*, 579, A108
- Maíz Apellániz, J. et al. 2015b, *A&A*, 583, A132
- Maíz Apellániz, J. et al. 2016, *ApJS*, 224, 4
- Maíz Apellániz, J. et al. 2017, *MNRAS*, 464, 3561
- Maíz Apellániz, J. et al. 2018a, *A&A*, 615, A161
- Maíz Apellániz, J. et al. 2018b, *A&A*, 616, A149
- Maíz Apellániz, J. et al. 2019a, in *HSA 10*, 420
- Maíz Apellániz, J. et al. 2019b, *A&A*, 626, A20 (MONOS I)
- Maíz Apellániz, J. et al. 2020, *A&A*, 643, A138
- Maíz Apellániz, J. et al. 2021a, *MNRAS*, 501, 2487
- Maíz Apellániz, J. et al. 2021b, *A&A*, 646, A11
- Maíz Apellániz, J. et al. 2021c, *A&A*, 649, A13
- Maíz Apellániz, J. et al. 2022, *A&A*, 657, A72
- Markwardt, C. B. 2009, in *ASP Conference Series*, Vol. 411, 251
- Martín-Ravelo, P. et al. 2024, *A&A*, 690, A306
- Mason, B. D., Gies, D. R., Hartkopf, W. I., et al. 1998, *AJ*, 115, 821
- Mason, B. D. et al. 2001, *AJ*, 122, 3466
- Molina Calzada, J. A. & Maíz Apellániz, J. 2025, arXiv:2510.23338
- Mowlavi, N., Holl, B., Lecoœur-Taïbi, I., et al. 2023, *A&A*, 674, A16
- Nazé, Y., Damerdjji, Y., Rauw, G., et al. 2010, *ApJ*, 719, 634
- Negueruela, I., Maíz Apellániz, J., et al. 2015, in *HSA 8*, 524–529
- Oka, T., Welty, D. E., Johnson, S., et al. 2013, *ApJ*, 773, 42
- Pantaleoni González, M., Maíz Apellániz, J., et al. 2021, *MNRAS*, 504, 2968
- Pantaleoni González, M., Maíz Apellániz, J., et al. 2025, *MNRAS*, 543, 63
- Prusti, T., de Bruijne, J. H. J., Brown, A. G. A., et al. 2016, *A&A*, 595, A1
- Puls, J., Urbaneja, M. A., Venero, R., et al. 2005, *A&A*, 435, 669
- Putkuri, C., Gamen, R., Benvenuto, O. G., et al. 2022, *MNRAS*, 517, 3101
- Putkuri, C., Gamen, R., Morrell, N. I., et al. 2021, *A&A*, 650, A96
- Putkuri, C., Gamen, R., Morrell, N. I., et al. 2023, *MNRAS*, 525, 6084
- Quintero, E. A., Eenens, P., & Rauw, G. 2020, *AN*, 341, 628
- Quirrenbach, A. et al. 2014, in *SPIE Conference Series*, Vol. 9147, 91471F
- Reed, B. C. 2003, *AJ*, 125, 2531
- Repolust, T., Puls, J., & Herrero, A. 2004, *A&A*, 415, 349
- Ricker, G. R. et al. 2015, *JATIS*, 1, 014003
- Rosu, S. 2022, PhD thesis, University of Liège
- Rosu, S. 2025, *Contrib. of the Astronomical Observatory Skalnaté Pleso*, 55, 81
- Rosu, S., Maíz Apellániz, J., Sciarini, L., et al. 2025, arXiv:2510.16202
- Rosu, S. et al. 2020a, *A&A*, 635, A145
- Rosu, S. et al. 2020b, *A&A*, 642, A221
- Rosu, S. et al. 2022a, *A&A*, 660, A120
- Rosu, S. et al. 2022b, *A&A*, 664, A98
- Rosu, S. et al. 2023, *MNRAS*, 521, 2988
- Sana, H., de Koter, A., de Mink, S. E., et al. 2013, *A&A*, 550, A107
- Sana, H., de Mink, S. E., de Koter, A., et al. 2012, *Science*, 337, 444
- Sana, H., Gosset, E., & Evans, C. J. 2009, *MNRAS*, 400, 1479
- Sana, H., Gosset, E., Nazé, Y., Rauw, G., & Linder, N. 2008, *MNRAS*, 386, 447
- Sana, H., James, G., & Gosset, E. 2011, *MNRAS*, 416, 817
- Sana, H., Le Bouquin, J.-B., Lacour, S., et al. 2014, *ApJS*, 215, 15
- Sana, H., Shenar, T., Bodensteiner, J., et al. 2025, *Nature Astronomy*, 9, 1337
- Sánchez-Bermúdez, J., Schödel, R., Alberdi, A., et al. 2013, *A&A*, 554, L4
- Santolaya-Rey, A. E., Puls, J., & Herrero, A. 1997, *A&A*, 323, 488
- Saydari, A. K. & Green, G. M. 2025, arXiv:2507.07162
- Schneider, N., Bontemps, S., Motte, F., et al. 2016, *A&A*, 591, A40
- Schultheis, M. et al. 2023, *A&A*, 674, A40
- Shenar, T., Bodensteiner, J., Abdul-Masih, M., et al. 2020, *A&A*, 639, L6
- Shenar, T., Bodensteiner, J., Sana, H., et al. 2024, *A&A*, 690, A289
- Shenar, T., Sana, H., Mahy, L., et al. 2022a, *Nature Astronomy*, 6, 1085
- Shenar, T., Sana, H., Mahy, L., et al. 2022b, *A&A*, 665, A148
- Simon, K. P. & Sturm, E. 1994, *A&A*, 281, 286
- Simón-Díaz, S., Caballero, J. A., Lorenzo, J., et al. 2015, *ApJ*, 799, 169
- Simón-Díaz, S. & Herrero, A. 2007, *A&A*, 468, 1063
- Simón-Díaz, S. & Herrero, A. 2014, *A&A*, 562, A135
- Simón-Díaz, S. et al. 2011a, *Journal of Physics Conference Series*, 328, 012021
- Simón-Díaz, S. et al. 2011b, in *Stellar Clusters & Associations*, 255–259
- Simón-Díaz, S. et al. 2024, arXiv:2405.11209
- Snow, T. P., Zukowski, D., & Massey, P. 2002, *ApJ*, 578, 877
- Sota, A., Maíz Apellániz, J., Morrell, N. I., et al. 2014, *ApJS*, 211, 10
- Sota, A., Maíz Apellániz, J., et al. 2008, in *RMxAC*, Vol. 33, 56
- Stroud, V. E., Clark, J. S., Negueruela, I., et al. 2010, *A&A*, 511, A84
- Trigueros Páez, E. et al. 2021, *A&A*, 655, A4 (MONOS II)
- Villaseñor, J. I., Sana, H., Mahy, L., et al. 2025, *A&A*, 698, A41
- Walborn, N. R. 1971, *ApJS*, 23, 257
- Walborn, N. R. 1972, *AJ*, 77, 312
- Walborn, N. R. 1973, *AJ*, 78, 1067
- Walborn, N. R. 1982, *AJ*, 87, 1300
- Walborn, N. R., Howarth, I. D., Lennon, D. J., et al. 2002, *AJ*, 123, 2754
- Weiler, M., Carrasco, J. M., Fabricius, C., & Jordi, C. 2023, *A&A*, 671, A52
- Wilson, O. C. 1937, *PASP*, 49, 338
- Zhang, R., Yuan, H., Huang, B., et al. 2024, *ApJ*, 971, 127
- Zhao, H., Schultheis, M., Qu, C., & Zwitter, T. 2024, *A&A*, 683, A199

Appendix A: Glossary

We provide a list of acronyms and terms used in this paper.

- a : (Orbital) semi-major axis.
- ALS: Alma Luminous Star catalog.
- BRJD: Barycentric Julian Date $-2.4 \cdot 10^6$ d.
- CAHA: Centro Astronómico Hispano-Alemán/Andaluz.
- CAHA2.2: CAHA 2.2 m telescope.
- CAHA3.5: CAHA 3.5 m telescope.
- CollDIBs: Collection of DIBs (Maíz Apellániz 2015).
- DIB: Diffuse Interstellar Band.
- DR3: (*Gaia*) third data release.
- DR4: (*Gaia*) fourth data release.
- e : (Orbital) eccentricity.
- ESO: European Southern Observatory.
- EW: Equivalent Width.
- FWHM: Full-Width at Half Maximum.
- GLS: Galactic Luminous Star.
- GOSC: Galactic O-Star Catalog.
- GOSSS: Galactic O-Star Spectroscopic Survey.
- GTC: Gran Telescopio Canarias.
- γ : Systemic velocity.
- HET: Hobby-Eberly Telescope.
- i : (Orbital or rotational) inclination.
- IFU: Integral Field Unit.
- ISM: Interstellar Medium.
- K : Semi-amplitude of the RV curve.
- \mathcal{L} : Spectroscopic luminosity ($= T_{\text{eff}}^4/g$).
- LiLiMaRlin: Library of Libraries of Massive-Star High-Resolution Spectra.
- $\log Q$: Wind-strength parameter (Holgado et al. 2018).
- M_{spec} : Spectroscopic mass.
- M_{evol} : Initial evolutionary mass.
- MT: Mercator Telescope.
- M³W: Multiplicity of Massive stars in the Milky Way.
- NOT: Nordic Optical telescope.
- ω : Argument of periastron.
- OHP: Observatoire de Haute-Provence.
- OLS2.2: Observatorio de La Silla 2.2 m telescope
- OLS3.6: Observatorio de La Silla 3.6 m telescope.
- ORM: Observatorio del Roque de los Muchachos.
- P : (Orbital) period.
- q : Mass ratio.
- RV(S): Radial Velocity (Spectrometer).
- SB1(E): Single-lined spectroscopic (Eclipsing) Binary.
- SB2(E): Double-lined spectroscopic (Eclipsing) Binary.
- SED: Spectral Energy Distribution.
- T_0 : Time of periastron passage.
- Θ_{RT} : Macroturbulent velocity.
- TNG: Telescopio Nazionale Galileo.
- VLT: Very Large Telescope.
- WDS: Washington Double Star catalog (Mason et al. 2001).
- WHT: William Herschel Telescope.
- (ZA)MS: Zero-Age Main Sequence.

Appendix B: The DIB catalog

B.1. Building the catalog

We present the details of the DIB catalog associated with UNWIND and this paper. To build the catalog we used six ISM standard stars (one primary and five secondary):

- *GLS 11 448* is the object of study of section 4 in this paper and is our primary ISM standard for three reasons: high

Table B.1. Information for the six ISM standard stars

Star	ID	Spectral type	RV (km/s)
GLS 11 448	1	O3.5 II(f*) + O3.5 II(f*)	-14.9±2.0
Cyg OB2-12	2	B5 Ia+	-9.2±1.6
HD 183 143	3	B8 Iae	-0.6±3.8
V747 Cep	4	O5.5 V(n)((f))	-15.6±1.7
ζ Oph	5	O9.2 IVnn(e)	-14.8±2.0
σ Sco Aa,Ab	6	B0.7 IV + B1: V	-7.3±1.8

- extinction, very scarce presence of stellar features due to the early-O spectral types of its two components, and its SB2 nature (which allows for an additional differentiation between stellar and ISM features using multi-epoch spectroscopy).
- *Cyg OB2-12* is selected due to its even higher extinction than GLS 11 448 and its contrast in spectral classification to the primary standard, as it is a late-B hypergiant with few stellar features in common with it other than H and some He I lines. We note its higher number of stellar features and variability.
 - *HD 183 143* is a late-B supergiant that has been previously used as an ISM standard. Its presence allows for the verification of some DIBs and a comparison with previous results.
 - *V747 Cep* is another obscured early-O spectroscopic binary that we use to verify some of the DIBs seen only in the primary standard (avoiding contamination by stellar lines in the two B stars above) that has the advantage of being in an H II region (Berkeley 59), thus probing a different environment.
 - ζ Oph is a fast-rotating late-O runaway star that has a significantly lower extinction than the first four standards. It is included here because it is the prototype for (quasi-)single-kinematic-component low-UV-exposure ISM sightlines (so-called ζ sightlines after it, Krelowski et al. 1997).
 - σ Sco Aa,Ab is the counterpart of ζ Oph for (quasi-)single-kinematic-component ISM sightlines for the high-UV exposure case (σ sightlines, Krelowski et al. 1997). It is a visual double with a Hipparcos separation of 0'.428 and with Aa being itself an SB2 system (Maíz Apellániz et al. 2021b). Our data includes the combined light of the three stars.

We used the multi-epoch high-resolution LiLiMaRlin spectroscopy to produce high-S/N spectra of the six standards. Before analysing the DIBs, we studied different ISM lines with well known wavelengths (Na I λ 5889.951, 5895.924; Ca II λ 3933.633, 3968.468; K I λ 7664.911, 7698.974; CH λ 4300.313; and C₂ λ 8761.194) to determine the average velocity of each ISM sightline (Fig. B.1 and Table B.1) and, in that way, measure the DIB central wavelengths λ_0 with respect to the ISM rest frame. While the ζ Oph and σ Sco Aa,Ab sightlines are dominated by a single cloud (with weak secondary components that are unlikely to contribute much for DIBs), the other four are more complex. GLS 11 448, Cyg OB2-12, and HD 183 143 have (at least) two main kinematic components and V747 Cep has a broad main component and a weak secondary one. This is important for narrow DIBs with possible intrinsic level structure (Galazutdinov et al. 2002; Bernstein et al. 2018), where the fitted DIB profiles should appear kinematically broadened for those four stars.

Given the different wavelength ranges of the LiLiMaRlin spectra as well as for practical purposes, we divided the full wavelength range to be analysed (4000-17 100 Å) into smaller ranges of ~ 100 Å each (increasing or decreasing the value as convenient and setting the limits at regions of featureless continuum) and processed them independently with UNWIND. We

Table B.2. DIBs used for the UNWIND database, with their average λ_0 and FWHM, the EW measured for GLS 11 448, and the number of gaussians (n_G) and stars (IDs in Table B.1) used to determine the profile.

Name	λ_0 (Å)	FWHM (Å)	EW (mÅ)	n_G	Stars used	Name	λ_0 (Å)	FWHM (Å)	EW (mÅ)	n_G	Stars used	Name	λ_0 (Å)	FWHM (Å)	EW (mÅ)	n_G	Stars used
DIBB4075	4074.7	10.5	156	1	123	DIBI5671	5671.1	9.9	75	1	14	DIBN5986	5986.44	0.66	2	1	1234
DIBB4179	4178.7	20.8	230	1	123	DIBB5705	5704.8	12.3	150	1	124	DIBN5988	5988.08	0.77	8	1	12345
DIBN4259	4258.95	1.29	5	1	134	DIBN5705	5705.16	2.39	98	1	123456	DIBN5989	5989.42	0.53	5	1	1234
DIBN4364	4363.82	0.47	8	1	14	DIBN5708	5707.67	0.47	3	1	125	DIBN5996	5995.79	0.73	6	1	1234
DIBN4372	4371.68	2.77	34	1	1234	DIBN5710	5710.46	0.66	6	1	1245	DIBN6000	5999.80	0.84	5	1	1234
DIBB4429	4428.8	17.7	1962	2	134	DIBN5711	5711.39	0.68	10	1	1245	DIBN6005	6005.08	2.65	43	1	123456
DIBN4495	4494.74	2.20	31	1	1356	DIBN5716	5716.23	0.38	2	1	145	DIBN6010	6010.48	4.18	147	1	123456
DIBN4502	4501.93	2.99	170	3	156	DIBN5720	5719.60	0.66	17	2	14	DIBN6015	6014.98	1.01	3	1	123456
DIBB4590	4590.3	23.1	283	1	13	DIBN5741	5741.36	2.33	29	1	14	DIBN6019	6019.41	1.01	15	1	12346
DIBN4727	4726.85	2.42	234	2	14	DIBN5745	5744.56	1.34	16	1	14	DIBN6024	6023.59	1.28	3	1	1234
DIBB4761	4761.2	19.1	444	1	13	DIBN5747	5746.89	1.86	30	1	14	DIBN6027	6027.38	1.63	24	1	123456
DIBN4763	4762.57	2.10	112	2	34	DIBN5749	5748.94	1.99	19	1	14	DIBI6037	6037.1	5.8	118	1	1234
DIBN4780	4780.44	1.56	115	2	1	DIBN5763	5762.65	0.58	5	1	123456	DIBN6037	6037.34	1.34	13	1	123456
DIBB4884	4883.7	16.7	861	2	1234	DIBN5766	5765.91	0.74	21	2	1345	DIBI6045	6045.4	7.5	107	1	1234
DIBN4947	4947.21	0.53	3	1	23	DIBN5769	5769.05	0.43	7	1	1234	DIBN6051	6051.37	0.62	2	1	1234
DIBN4951	4951.19	0.87	5	1	12345	DIBN5773	5772.58	1.50	20	1	1234	DIBN6057	6057.33	0.55	3	1	12345
DIBN4957	4956.60	1.10	1	1	3456	DIBN5776	5775.86	0.83	7	1	12346	DIBN6059	6059.21	0.56	5	1	1234
DIBN4964	4963.87	0.62	37	1	12345	DIBI5778	5778.4	8.2	245	1	123456	DIBN6060	6060.13	0.69	7	1	12346
DIBN4969	4969.06	0.76	8	1	12345	DIBN5781	5780.69	2.06	522	2	123456	DIBN6065	6065.19	0.65	11	1	123456
DIBN4980	4979.55	0.64	9	1	14	DIBN5785	5784.98	1.19	19	1	1234	DIBN6068	6068.07	1.35	8	1	1234
DIBN4982	4982.13	0.32	2	1	123	DIBN5788	5788.05	3.47	58	1	13456	DIBN6071	6071.18	0.99	6	1	1234
DIBN4985	4984.77	0.50	16	1	12346	DIBN5793	5793.18	1.27	17	1	134	DIBN6081	6081.02	0.44	2	1	12345
DIBN4988	4987.65	0.97	4	1	12346	DIBN5795	5795.38	1.82	42	1	123456	DIBN6085	6084.81	0.85	6	1	12345
DIBN5004	5003.57	0.94	13	1	14	DIBN5797	5797.23	0.70	189	4	156	DIBN6090	6089.80	0.60	16	1	123456
DIBN5028	5027.53	0.63	5	1	134	DIBN5801	5800.96	2.74	20	1	1235	DIBN6099	6098.54	0.62	4	1	12345
DIBN5055	5054.80	0.48	4	1	124	DIBN5807	5806.50	1.21	5	1	136	DIBN6103	6102.65	0.87	2	1	12345
DIBN5062	5061.52	0.49	10	1	12345	DIBN5809	5809.28	1.45	35	1	12356	DIBN6106	6106.33	0.70	3	1	12345
DIBN5074	5074.47	0.55	7	1	145	DIBN5812	5811.91	1.65	19	1	12356	DIBN6107	6107.25	0.61	4	1	12345
DIBN5092	5092.05	0.79	3	1	2345	DIBN5814	5814.21	0.49	3	1	123456	DIBN6108	6108.04	0.46	10	1	123456
DIBI5111	5111.1	5.7	46	1	12345	DIBN5816	5815.77	0.53	2	1	123456	DIBN6110	6109.88	0.60	4	1	12345
DIBI5154	5154.1	6.0	41	1	134	DIBN5819	5818.66	0.63	5	1	123456	DIBN6113	6113.14	0.83	23	1	123456
DIBN5170	5170.47	0.35	4	1	245	DIBN5821	5821.10	0.30	1	1	12456	DIBN6117	6116.79	0.92	14	1	123456
DIBN5176	5175.98	0.61	14	1	123456	DIBN5828	5828.48	0.73	11	1	123456	DIBN6119	6118.53	0.62	5	1	12345
DIBN5236	5236.16	1.49	33	1	12456	DIBN5838	5838.01	0.33	3	1	123456	DIBN6128	6128.43	2.18	10	1	1234
DIBI5246	5245.8	5.7	74	1	12345	DIBN5841	5840.61	0.58	2	1	123456	DIBN6133	6133.39	0.76	3	1	1346
DIBN5299	5299.45	4.24	42	1	1245	DIBN5844	5843.73	4.26	58	1	123456	DIBN6136	6135.78	1.24	5	1	1234
DIBN5340	5340.24	0.63	5	1	1234	DIBN5845	5844.89	0.65	9	1	123456	DIBN6140	6139.92	0.66	12	1	123456
DIBN5359	5358.80	0.28	1	1	14	DIBN5850	5849.75	0.93	70	1	123456	DIBN6142	6142.31	0.99	5	1	124
DIBN5364	5363.72	2.10	36	1	123456	DIBN5854	5854.38	0.54	4	1	13456	DIBN6146	6145.67	0.58	3	1	12456
DIBN5404	5404.49	0.90	20	1	12346	DIBN5856	5855.54	0.49	3	1	123456	DIBN6148	6148.23	1.04	6	1	123456
DIBN5419	5418.84	0.72	24	1	12345	DIBN5859	5859.11	2.03	4	1	123	DIBN6151	6150.83	1.26	8	1	123456
DIBN5424	5424.17	0.94	6	1	123456	DIBN5885	5885.32	0.48	2	1	14	DIBN6157	6157.18	2.70	1	1	236
DIBB5449	5449.0	12.1	253	1	1234	DIBN5894	5893.50	0.47	4	1	124	DIBN6159	6158.52	0.74	5	1	2345
DIBN5487	5487.40	4.57	129	1	123456	DIBN5900	5900.43	0.76	10	1	1234	DIBN6162	6161.83	0.39	6	1	123456
DIBN5494	5494.05	0.57	27	1	123456	DIBN5905	5904.58	0.69	2	1	124	DIBN6164	6163.56	0.66	3	1	123456
DIBN5497	5497.02	2.13	10	1	1235	DIBN5908	5907.81	0.98	4	1	1246	DIBN6166	6165.61	1.33	7	1	1234
DIBN5503	5503.02	0.72	3	1	123	DIBN5911	5910.51	0.84	15	1	123456	DIBN6168	6167.79	0.47	1	1	123
DIBN5504	5504.26	0.50	4	1	123	DIBN5914	5913.73	0.47	2	1	1345	DIBN6171	6170.59	1.02	2	1	1234
DIBN5506	5506.09	0.97	19	1	1245	DIBN5915	5914.69	0.42	1	1	145	DIBN6175	6174.59	0.43	1	1	1245
DIBN5508	5508.15	2.08	63	1	12456	DIBN5917	5916.99	1.33	10	1	12345	DIBB6176	6176.2	23.9	1007	2	123456
DIBN5513	5512.65	0.57	13	1	123456	DIBN5922	5922.23	0.35	3	1	1234	DIBN6178	6177.80	1.49	8	1	124
DIBN5516	5515.93	0.69	3	1	12346	DIBN5923	5923.16	0.64	18	1	12345	DIBN6183	6182.61	0.74	1	1	12346
DIBI5525	5524.9	6.7	54	1	12346	DIBN5924	5924.14	0.95	10	1	12345	DIBN6186	6185.80	0.61	6	1	12346
DIBN5535	5535.28	1.78	42	1	123456	DIBN5926	5925.83	0.85	16	1	12345	DIBN6187	6187.20	1.04	10	1	12346
DIBN5538	5537.70	1.09	8	1	134	DIBN5928	5927.64	0.51	5	1	12345	DIBN6189	6189.38	0.58	4	1	12345
DIBN5542	5541.80	0.69	10	1	12345	DIBN5945	5945.44	0.62	2	1	123456	DIBN6195	6194.68	0.54	10	1	123456
DIBN5545	5544.99	0.77	27	1	123456	DIBN5947	5947.22	0.58	7	1	123456	DIBN6196	6195.94	0.52	68	1	123456
DIBN5546	5546.38	0.80	10	1	12345	DIBN5949	5948.87	0.39	2	1	123456	DIBN6199	6198.90	0.70	7	1	1234
DIBN5547	5547.37	0.35	2	1	124	DIBN5952	5952.27	0.55	1	1	12456	DIBN6203	6202.83	1.31	103	2	123456
DIBN5601	5600.54	1.26	6	1	12346	DIBN5954	5954.20	0.26	1	1	123456	DIBI6204	6204.0	5.5	211	1	123456
DIBN5610	5609.75	2.26	33	1	12346	DIBN5958	5958.48	0.47	10	1	12456	DIBN6204	6204.38	0.97	2	1	123456
DIBN5635	5634.77	1.05	8	1	1234	DIBN5959	5959.12	0.57	12	1	12456	DIBN6212	6211.63	0.53	6	1	123456
DIBN5640	5640.31	0.63	5	1	14	DIBN5963	5962.53	1.46	8	1	123456	DIBN6213	6212.91	0.52	2	1	12345
DIBN5644	5643.51	3.60	19	1	14	DIBN5974	5973.78	0.47	3	1	123456	DIBN6223	6223.49	0.46	4	1	123456
DIBN5645	5645.43	0.41	2	1	14	DIBN5976	5975.69	0.36	3	1	123456	DIBN6226	6226.18	0.49	4	1	12346
DIBN5652	5652.01	1.09	6	1	124	DIBN5983	5982.86	1.24	10	1	12345	DIBN6234	6233.98	0.60	15	1	123456

Table B.2. (Continued).

Name	λ_0 (Å)	FWHM (Å)	EW (mÅ)	n_G	Stars used	Name	λ_0 (Å)	FWHM (Å)	EW (mÅ)	n_G	Stars used	Name	λ_0 (Å)	FWHM (Å)	EW (mÅ)	n_G	Stars used
DIBN6237	6236.71	0.55	6	1	123456	DIBN6600	6599.84	0.51	2	1	123	DIBN6822	6821.57	1.45	8	1	1234
DIBN6244	6244.48	0.80	8	1	123456	DIBN6607	6606.95	0.79	6	1	123	DIBN6823	6823.38	0.41	4	1	1234
DIBN6245	6245.28	0.59	6	1	12346	DIBN6614	6613.71	0.96	226	4	56	DIBN6827	6827.28	0.81	10	1	123456
DIBN6251	6250.85	0.62	5	1	123456	DIBN6621	6621.48	0.53	3	1	12345	DIBN6834	6834.31	0.68	3	1	12345
DIBN6252	6252.35	0.38	1	1	1234	DIBN6623	6622.75	0.56	10	1	12345	DIBN6838	6837.61	0.84	9	1	1234
DIBN6260	6259.62	0.56	2	1	12345	DIBN6625	6624.79	0.60	3	1	12345	DIBN6839	6839.41	0.55	3	1	12345
DIBN6266	6266.44	1.42	7	1	123456	DIBN6626	6625.83	0.66	3	1	12345	DIBN6842	6841.56	0.69	12	1	1235
DIBN6270	6269.83	1.27	140	2	123456	DIBN6628	6628.02	0.95	4	1	12345	DIBN6844	6843.51	1.09	33	1	123456
DIBN6278	6277.99	3.02	174	1	1234	DIBN6631	6630.72	0.51	4	1	12345	DIBN6845	6845.31	0.55	4	1	123456
DIBN6280	6280.31	1.46	73	1	1234	DIBN6632	6631.55	0.45	3	1	12345	DIBN6846	6846.40	0.40	2	1	1234
DIBN6284	6284.04	3.31	974	3	1234	DIBN6633	6632.73	1.01	13	1	12346	DIBN6848	6847.59	0.56	3	1	123
DIBN6288	6287.52	0.74	14	1	12346	DIBN6635	6635.19	0.34	1	1	1234	DIBN6852	6852.43	0.73	11	1	123456
DIBN6289	6289.19	2.70	117	1	12346	DIBN6636	6635.59	0.46	2	1	12345	DIBN6860	6860.00	0.68	12	1	123456
DIBN6302	6302.40	1.45	27	1	1456	DIBN6638	6637.53	0.36	1	1	12345	DIBN6862	6862.47	0.47	5	1	123456
DIBI6309	6309.1	7.2	281	1	145	DIBN6639	6639.27	0.61	3	1	12345	DIBN6878	6877.57	0.91	16	1	1234
DIBN6309	6309.42	1.29	16	1	1246	DIBN6643	6643.42	1.45	11	1	12345	DIBN6887	6886.89	0.89	12	1	1234
DIBI6317	6317.4	7.4	256	1	145	DIBN6646	6645.92	0.81	6	1	12345	DIBN6900	6900.30	0.96	7	1	13
DIBN6318	6318.22	0.53	7	1	146	DIBN6655	6654.68	0.58	3	1	12345	DIBN6904	6903.86	0.49	4	1	1234
DIBN6325	6324.75	0.86	22	1	12346	DIBN6657	6657.21	0.67	4	1	1234	DIBN6905	6905.01	1.41	14	1	1234
DIBN6330	6330.01	0.80	10	1	123456	DIBN6659	6658.63	0.51	2	1	12345	DIBN6914	6913.69	2.06	30	1	1234
DIBN6346	6346.08	1.28	9	1	146	DIBN6661	6660.63	0.61	31	1	123456	DIBN6919	6919.09	0.93	38	1	1234
DIBN6349	6349.39	0.42	3	1	14	DIBN6662	6662.00	0.56	4	1	12345	DIBN6927	6926.67	1.07	9	1	1234
DIBN6353	6353.28	1.66	27	1	12346	DIBN6664	6663.94	0.83	6	1	12345	DIBN6930	6929.87	2.11	29	1	124
DIBN6358	6358.31	0.60	4	1	12346	DIBN6665	6665.17	0.66	7	1	12345	DIBB6937	6936.5	12.1	204	1	123456
DIBN6362	6362.27	1.74	25	1	12346	DIBN6669	6669.43	0.92	6	1	1234	DIBN6945	6944.56	0.96	23	1	1234
DIBN6367	6367.26	0.47	13	1	123456	DIBN6672	6672.17	0.73	20	1	12346	DIBN6947	6946.72	1.88	9	1	1234
DIBN6369	6369.11	1.45	14	1	1456	DIBN6674	6673.92	0.75	4	1	1234	DIBN6951	6950.51	0.65	8	1	1236
DIBN6376	6375.95	0.56	25	1	123456	DIBN6685	6684.71	0.97	9	1	1234	DIBN6952	6951.71	0.47	6	1	1234
DIBN6377	6376.84	1.91	28	1	123456	DIBN6686	6686.44	0.50	2	1	1234	DIBN6971	6971.43	1.16	10	1	123456
DIBN6379	6379.23	0.68	86	1	123456	DIBN6689	6689.25	0.92	8	1	1234	DIBN6974	6973.59	0.55	8	1	1234
DIBN6397	6396.89	1.14	19	1	12456	DIBN6694	6693.65	0.57	3	1	12345	DIBN6978	6978.33	0.79	7	1	12345
DIBN6400	6400.38	0.70	5	1	145	DIBN6695	6694.50	0.62	6	1	1234	DIBN6982	6982.24	0.91	8	1	123456
DIBB6407	6406.6	10.1	294	1	145	DIBN6697	6696.90	0.50	2	1	12346	DIBN6993	6993.14	0.80	91	2	123456
DIBN6410	6410.09	1.05	12	1	145	DIBN6699	6699.22	0.72	25	1	12346	DIBN6997	6996.79	0.60	4	1	1234
DIBN6414	6413.52	3.06	34	1	12345	DIBN6702	6701.99	0.71	12	1	12346	DIBN6999	6998.66	0.98	13	1	1234
DIBN6419	6418.53	0.53	4	1	123456	DIBN6709	6709.40	0.92	11	1	1234	DIBN7002	7002.25	1.07	13	1	1234
DIBN6426	6425.64	0.64	15	1	12345	DIBN6713	6713.47	0.76	6	1	1234	DIBN7004	7004.31	0.39	2	1	1234
DIBN6438	6438.24	0.75	5	1	12346	DIBN6729	6729.16	0.90	15	1	12345	DIBN7020	7020.41	2.05	16	1	123456
DIBN6439	6439.44	0.70	20	1	123456	DIBN6733	6733.26	0.93	8	1	12345	DIBN7025	7025.14	1.14	14	1	1234
DIBN6443	6442.58	1.37	7	1	12356	DIBN6737	6737.16	0.64	6	1	123456	DIBN7030	7030.18	0.73	7	1	12346
DIBN6445	6445.24	0.77	34	1	12346	DIBN6741	6740.91	1.09	12	1	12345	DIBN7031	7031.47	0.56	7	1	12346
DIBN6449	6449.18	0.85	23	1	123456	DIBN6742	6742.49	0.90	8	1	1234	DIBN7046	7045.81	0.66	9	1	1234
DIBN6456	6455.97	1.21	34	1	123456	DIBN6744	6743.56	1.22	8	1	12345	DIBN7061	7060.98	0.60	19	1	12346
DIBN6460	6460.30	0.65	3	1	123456	DIBN6748	6747.72	0.87	7	1	12346	DIBN7063	7062.65	0.57	20	1	12345
DIBN6464	6463.59	1.00	13	1	123456	DIBN6751	6750.69	1.27	10	1	12345	DIBN7069	7069.45	1.13	28	1	1234
DIBN6465	6465.41	0.28	1	1	124	DIBN6752	6752.33	1.09	8	1	12345	DIBN7078	7077.99	1.07	14	1	1234
DIBN6467	6466.83	0.54	5	1	12346	DIBN6756	6755.73	1.23	3	1	1234	DIBN7080	7080.03	1.01	6	1	1234
DIBN6469	6468.66	0.85	7	1	123456	DIBN6757	6757.18	0.91	3	1	1234	DIBN7084	7083.65	0.92	7	1	1234
DIBN6474	6474.18	0.73	7	1	1234	DIBN6759	6759.12	1.11	2	1	12345	DIBN7085	7085.25	1.45	17	1	1234
DIBN6477	6476.95	0.55	3	1	1234	DIBN6762	6762.04	0.60	2	1	123	DIBN7087	7086.69	0.45	5	1	1234
DIBN6483	6483.38	0.54	4	1	145	DIBN6765	6765.24	0.67	2	1	12345	DIBN7093	7092.51	0.62	3	1	1234
DIBN6484	6484.33	0.61	4	1	15	DIBN6768	6767.66	0.57	2	1	12346	DIBN7096	7096.33	0.56	4	1	1234
DIBN6489	6489.49	1.06	9	1	123456	DIBN6770	6770.11	0.57	8	1	12345	DIBN7101	7101.26	0.79	2	1	124
DIBN6492	6491.96	0.53	12	1	12346	DIBN6779	6778.94	0.59	5	1	12345	DIBN7105	7105.18	0.59	4	1	1234
DIBI6494	6494.1	6.5	123	1	12346	DIBN6781	6780.63	0.76	4	1	12345	DIBN7116	7116.32	0.89	13	1	123456
DIBN6498	6497.88	0.69	6	1	12345	DIBN6786	6786.48	0.54	2	1	12346	DIBN7120	7119.77	1.32	25	1	123456
DIBN6517	6516.77	0.57	5	1	1234	DIBN6789	6788.75	0.71	7	1	12345	DIBN7124	7124.08	1.25	4	1	1234
DIBN6521	6520.54	0.98	23	1	12345	DIBN6792	6792.46	0.72	7	1	123456	DIBN7137	7136.78	1.29	8	1	1234
DIBN6536	6536.43	0.73	5	1	123456	DIBN6795	6795.18	0.63	9	1	123456	DIBN7138	7138.36	0.75	5	1	1234
DIBN6538	6537.57	0.64	1	1	12346	DIBN6801	6801.35	0.75	10	1	1234	DIBN7139	7139.09	3.72	31	1	124
DIBN6543	6543.04	0.60	6	1	12345	DIBN6803	6803.20	0.67	6	1	12345	DIBN7143	7142.94	0.60	3	1	1234
DIBN6549	6548.94	0.48	4	1	1234	DIBN6804	6804.30	1.29	7	1	12345	DIBN7154	7153.97	1.01	10	1	1234
DIBN6554	6553.80	0.48	7	1	1234	DIBN6809	6809.37	0.40	1	1	1234	DIBN7159	7159.32	0.57	8	1	1234
DIBI6590	6590.4	7.7	162	1	1234	DIBN6811	6811.06	0.60	8	1	123	DIBN7160	7160.04	0.84	5	1	1234
DIBN6594	6594.25	0.86	5	1	1234	DIBN6812	6811.74	1.11	10	1	123	DIBN7163	7162.85	0.52	5	1	1234
DIBN6597	6597.28	0.52	11	1	123456	DIBN6813	6812.82	0.81	8	1	1235	DIBN7166	7166.38	0.82	4	1	12
DIBN6599	6598.87	0.80	1	1	23	DIBN6818	6818.36	1.12	5	1	1234	DIBN7198	7198.46	0.75	5	1	123456

Table B.2. (Continued).

Name	λ_0 (Å)	FWHM (Å)	EW (mÅ)	n_G	Stars used	Name	λ_0 (Å)	FWHM (Å)	EW (mÅ)	n_G	Stars used	Name	λ_0 (Å)	FWHM (Å)	EW (mÅ)	n_G	Stars used
DIBN7204	7203.54	0.61	14	1	1234	DIBN7707	7706.69	0.76	7	1	123456	DIBN9988	9987.99	1.26	10	1	1234
DIBN7224	7224.06	1.24	239	2	12356	DIBN7708	7708.06	0.69	9	1	12346	DIBN9990	9989.56	4.39	19	1	123456
DIBN7228	7228.30	1.24	17	1	123456	DIBN7722	7721.90	0.73	23	1	123456	DIBN10004	10004.29	1.27	7	1	12346
DIBN7232	7231.59	1.30	18	1	1234	DIBI7748	7748.0	7.3	81	1	123456	DIBN10007	10006.78	1.35	10	1	12346
DIBN7249	7249.18	1.64	21	1	1234	DIBN7758	7758.33	2.79	14	1	123	DIBN10009	10008.57	3.20	16	1	1236
DIBN7258	7257.50	1.01	12	1	1234	DIBN7761	7761.40	2.84	20	1	123	DIBN10080	10080.30	2.31	11	1	12456
DIBN7268	7268.19	1.00	6	1	1234	DIBB7779	7779.4	12.2	111	1	12345	DIBN10162	10162.14	1.30	12	1	123
DIBN7274	7273.71	0.74	7	1	1234	DIBN7780	7780.37	0.76	1	1	12345	DIBN10208	10208.03	0.71	4	1	123
DIBN7275	7274.93	0.68	12	1	1234	DIBN7828	7827.64	0.77	6	1	1234	DIBN10233	10233.12	2.99	16	1	123456
DIBN7277	7276.55	0.68	18	1	1234	DIBN7829	7829.02	0.75	2	1	1234	DIBN10259	10258.80	1.43	6	1	12
DIBN7301	7300.95	0.81	8	1	1234	DIBN7833	7832.79	0.70	19	1	123456	DIBN10263	10262.60	1.23	11	1	1234
DIBN7303	7302.93	0.85	8	1	1234	DIBN7841	7840.80	0.68	5	1	1234	DIBN10280	10280.46	1.05	9	1	123
DIBN7322	7321.88	0.61	4	1	1234	DIBN7844	7843.54	1.74	4	1	14	DIBN10283	10283.15	0.85	5	1	1234
DIBN7330	7329.91	1.57	11	1	123	DIBI7844	7844.3	8.0	42	1	12346	DIBN10284	10284.35	0.55	5	1	124
DIBN7334	7334.39	0.97	39	1	12346	DIBN7846	7845.64	0.82	3	1	1234	DIBN10288	10288.35	1.19	12	1	1234
DIBN7340	7340.02	1.29	5	1	1234	DIBN7856	7855.91	0.77	2	1	1234	DIBN10327	10327.31	1.46	9	1	12346
DIBN7343	7342.58	1.91	11	1	1234	DIBN7862	7862.33	0.72	8	1	1234	DIBN10391	10391.30	0.56	2	1	124
DIBN7347	7347.20	2.05	25	1	12346	DIBN7866	7866.39	1.09	5	1	1234	DIBN10393	10393.31	1.07	16	2	124
DIBN7350	7349.75	1.06	25	1	123456	DIBI7874	7874.3	5.0	32	1	1234	DIBN10409	10409.03	0.91	5	1	1234
DIBN7355	7354.78	0.85	7	1	12346	DIBN7905	7904.78	1.63	7	1	1234	DIBN10439	10438.57	3.46	45	1	12345
DIBN7357	7357.45	1.31	44	1	12346	DIBN7915	7915.08	1.08	3	1	1234	DIBN10459	10458.71	2.67	18	1	12345
DIBN7361	7360.56	0.76	12	1	12346	DIBB7928	7927.6	10.0	157	1	1234	DIBN10476	10476.45	2.20	8	1	1234
DIBN7364	7363.83	0.47	4	1	1234	DIBN7935	7934.68	0.47	4	1	123	DIBN10505	10504.51	1.60	59	1	12345
DIBN7366	7366.10	1.11	23	1	123456	DIBN7936	7935.50	0.73	4	1	123	DIBN10507	10507.18	1.58	49	1	12345
DIBN7367	7367.07	0.55	27	1	123456	DIBN7943	7943.07	1.20	3	1	1234	DIBN10522	10521.54	3.29	8	1	1234
DIBN7376	7375.82	0.68	13	1	12346	DIBN7948	7947.67	1.78	9	1	1234	DIBN10528	10528.47	1.17	5	1	1234
DIBN7382	7382.43	1.11	8	1	1234	DIBN7951	7951.23	1.51	9	1	1234	DIBN10563	10562.72	2.77	8	1	1234
DIBN7386	7385.83	0.53	6	1	123456	DIBN7968	7967.59	2.41	5	1	1234	DIBN10568	10568.07	2.18	7	1	1234
DIBI7398	7398.1	5.3	22	1	12346	DIBN7971	7971.08	1.10	5	1	1234	DIBN10574	10573.60	4.17	27	1	12346
DIBN7402	7402.34	1.72	15	1	123456	DIBN8026	8026.17	0.71	27	1	12346	DIBN10579	10578.95	1.09	7	1	12346
DIBN7406	7405.53	0.68	7	1	123	DIBN8038	8037.52	2.30	38	1	1234	DIBN10610	10610.24	1.72	20	2	1234
DIBN7407	7406.82	1.68	16	1	123	DIBN8041	8040.73	2.10	18	1	1234	DIBN10615	10615.05	1.57	6	1	1234
DIBN7411	7410.69	1.69	4	1	1234	DIBN8099	8098.84	2.10	7	1	1234	DIBN10627	10627.29	0.91	2	1	12
DIBN7415	7414.60	0.89	1	1	123456	DIBN8105	8104.76	1.59	12	1	1234	DIBN10631	10630.71	1.35	3	1	1234
DIBN7419	7419.00	0.57	4	1	1234	DIBN8126	8125.92	1.15	9	1	1234	DIBN10634	10633.93	1.09	5	1	1256
DIBB7430	7430.4	16.3	213	1	123456	DIBN8155	8154.69	1.69	4	1	234	DIBN10643	10643.15	1.24	2	1	124
DIBN7451	7451.23	0.99	9	1	123456	DIBI8215	8215.3	8.3	42	1	14	DIBN10646	10646.17	0.91	3	1	126
DIBN7458	7458.21	1.10	3	1	123456	DIBI8258	8257.9	9.8	159	1	14	DIBN10650	10650.25	1.32	6	1	1234
DIBN7463	7462.81	2.77	15	1	12345	DIBI8278	8277.7	8.0	115	1	14	DIBN10698	10697.61	4.41	181	4	1246
DIBN7470	7470.30	0.71	8	1	124	DIBN8283	8283.14	1.42	38	1	1234	DIBN10703	10703.18	1.90	21	1	12346
DIBN7472	7472.46	0.67	5	1	1234	DIBI8314	8314.2	6.4	60	1	146	DIBN10731	10730.91	1.35	10	1	1234
DIBN7476	7476.43	1.22	6	1	1234	DIBN8409	8408.68	4.51	25	1	145	DIBN10735	10734.72	1.19	22	1	123456
DIBN7478	7478.39	1.07	7	1	12345	DIBN8420	8419.55	1.05	12	1	12346	DIBN10754	10753.57	1.48	5	1	12346
DIBN7483	7482.91	0.87	10	1	12345	DIBN8422	8422.09	0.97	2	1	12346	DIBN10757	10756.61	0.76	8	2	12346
DIBN7484	7483.99	0.55	5	1	12345	DIBN8439	8439.37	0.70	29	1	123456	DIBN10772	10772.19	3.17	25	1	123456
DIBN7493	7493.05	0.84	3	1	12345	DIBN8456	8456.09	0.78	3	1	1236	DIBN10775	10775.10	2.12	7	1	1236
DIBN7495	7494.92	0.59	14	1	123456	DIBN8458	8457.57	0.63	2	1	123	DIBN10781	10781.48	1.46	152	4	12346
DIBN7520	7520.46	0.92	6	1	123	DIBN8472	8471.63	0.43	2	1	146	DIBN10792	10792.47	1.75	54	2	12346
DIBN7532	7532.40	0.65	3	1	123	DIBN8530	8530.04	2.03	10	1	12456	DIBN10814	10813.71	1.71	14	1	12346
DIBN7535	7535.35	1.43	7	1	123	DIBN8571	8570.89	0.45	2	1	1234	DIBI10815	10815.1	6.8	56	1	12346
DIBN7544	7543.90	2.96	12	1	123	DIBN8572	8572.40	0.55	2	1	1234	DIBI10860	10859.7	6.0	39	1	1456
DIBI7558	7558.2	6.2	46	1	1234	DIBN8580	8580.03	1.59	13	1	14	DIBN10869	10868.79	1.53	6	1	12346
DIBN7558	7558.28	1.09	8	1	12346	DIBN8621	8620.99	3.99	314	2	123456	DIBN10877	10877.30	2.49	12	1	12346
DIBN7559	7559.27	0.71	13	1	2346	DIBI8646	8645.5	7.1	103	1	12346	DIBN10884	10884.07	1.30	16	1	12346
DIBN7562	7562.15	1.72	79	2	12356	DIBN8764	8763.54	0.70	2	1	36	DIBN10894	10893.97	2.66	25	1	12346
DIBN7564	7564.09	0.95	7	1	234	DIBI8781	8780.8	7.7	108	1	12345	DIBN11691	11691.18	1.98	44	1	123456
DIBN7568	7567.83	0.78	3	1	1234	DIBN8936	8935.56	1.92	20	1	124	DIBN11695	11695.15	1.10	17	1	1234
DIBI7569	7568.7	7.1	34	1	1234	DIBN9057	9057.30	2.02	16	1	1234	DIBN11700	11699.56	2.35	68	1	123456
DIBN7570	7570.04	1.27	6	1	1234	DIBN9366	9365.81	2.13	119	2	123	DIBN11709	11708.79	2.90	29	1	12456
DIBN7571	7571.45	0.54	4	1	1234	DIBN9429	9428.89	1.85	194	2	2	DIBN11721	11721.02	2.66	94	1	123456
DIBN7580	7579.56	1.07	17	1	123456	DIBN9577	9577.41	3.33	284	2	1234	DIBN11793	11793.02	2.25	33	1	12346
DIBN7581	7581.19	1.37	27	1	123456	DIBN9632	9631.94	2.37	190	2	1	DIBI11796	11796.3	5.6	65	1	123
DIBN7585	7585.47	1.18	5	1	23	DIBN9674	9673.51	1.25	13	2	123	DIBN11798	11797.78	1.60	147	2	12346
DIBI7687	7687.2	6.9	116	1	12346	DIBN9880	9880.37	0.96	37	2	1234	DIBN11971	11970.78	1.68	137	2	14
DIBN7696	7695.75	0.64	7	1	123	DIBN9888	9887.85	1.25	17	1	12345	DIBN12201	12200.83	1.95	14	1	12346
DIBU7697	7696.5	151.6	5445	1	1234	DIBN9892	9892.14	1.25	13	1	1234	DIBN12230	12230.18	1.41	18	1	12346
DIBN7704	7704.37	3.72	56	1	123456	DIBN9986	9986.25	1.08	6	1	1234	DIBN12268	12268.41	2.81	10	1	1234

Table B.2. (Continued).

Name	λ_0 (Å)	FWHM (Å)	EW (mÅ)	n_G	Stars used	Name	λ_0 (Å)	FWHM (Å)	EW (mÅ)	n_G	Stars used	Name	λ_0 (Å)	FWHM (Å)	EW (mÅ)	n_G	Stars used
DIBN12288	12 287.68	2.84	21	1	12346	DIBN12878	12 878.47	2.54	23	1	123456	DIBN15637	15 636.99	2.96	18	1	1236
DIBN12294	12 294.05	1.62	24	1	12346	DIBN12993	12 992.57	1.41	19	1	124	DIBI15647	15 647.3	5.2	100	2	234
DIBN12314	12 313.82	1.44	10	1	12346	DIBN12996	12 995.56	3.03	39	1	124	DIBN15932	15 932.32	3.23	13	1	12345
DIBN12407	12 406.70	1.87	15	1	1234	DIBN13021	13 020.70	1.58	32	1	124	DIBN16568	16 568.32	3.67	23	1	123456
DIBN12412	12 412.39	1.40	4	1	123	DIBN13026	13 025.92	2.58	44	1	124	DIBN16580	16 580.05	3.44	12	1	123
DIBN12519	12 519.27	3.00	28	1	123456	DIBI13028	13 028.3	6.4	88	1	124	DIBN16633	16 633.48	3.22	6	1	123
DIBN12538	12 538.11	3.25	61	2	1234	DIBN13052	13 051.58	2.29	12	1	1234	DIBI16918	16 917.5	5.5	79	1	123456
DIBN12624	12 624.25	1.87	48	1	1246	DIBN13176	13 176.29	3.89	559	2	12346	DIBN17063	17 063.42	3.42	31	1	123456
DIBN12650	12 649.94	3.85	28	1	126	DIBN15268	15 268.02	3.33	268	1	123456	DIBN17072	17 072.39	2.35	23	1	1234
DIBN12692	12 692.13	1.27	16	1	12	DIBN15612	15 611.66	4.57	65	3	23						
DIBN12799	12 799.12	1.44	29	1	1234	DIBN15620	15 620.46	1.67	14	1	123						

inspected each range to determine the main rectification points away from stellar, ISM, and telluric features and the additional rectification points (if needed) inside stellar lines with ISM absorption features. We first cleaned the LiLiMaRlin spectra (previously cleaned from telluric absorption by the pipeline for each telescope) from additional telluric features (when needed) and then we simultaneously fitted the standard ISM lines and DIBs.

The DIB fitting was done iteratively, fixing RV to that of the ISM rest frame but leaving λ_0 , FWHM and the EW free. For DIBs with asymmetries or internal level structure (e.g. DIBN6614) we fitted the profiles with multiple (2 to 4) Gaussians. We tried fitting each DIB in as many stars as possible, explicitly excluding the DIB-star combinations where the DIB was too weak or contaminated by stellar features. For cases with multiple Gaussians we were even more strict in the stars we selected, excluding those where some circumstance (e.g. kinematic broadening, see above) led to a poor fit. Finally, the λ_0 and FWHM of each fitted Gaussian was averaged among the selected stars in each case to yield the final parameters. The fact that a star was not selected to build the DIB parameters does not necessarily mean that the DIB is not detected for that star in our data, just that it does not meet the requirements described above.

We identify a total of 631 DIBs in the 4000-17 100 Å range (Table B.2). Each DIB is given a DIBXY name, with X identifying its width category [N(arrow): FWHM < 5 Å, I(termediate): between 5 and 10 Å, B(road): between 10 and 100 Å, and U(ltrabroad): FWHM > 100 Å] and Y being a 4-5 digits number with its central (air) wavelength in Å rounded to the nearest integer. A colour code is included in the DIB names to facilitate the identification of each category. For each DIB we give its preferred FWHM and λ_0 as well as the EW for GLS 11 448. We also give the number of Gaussians used to fit each DIB (with a colour code to identify cases with multiple Gaussians, see below) and the stars used to build each profile (with a colour code to identify new DIBs, see below).

Of the 631 DIBs in Table B.2, 37 are fitted with multiple Gaussians (examples in Fig. B.3) and their information is given in Table B.3. For each of those, we list the name, λ_0 , and FWHM from Table B.2 and also give the skewness and excess kurtosis (both zero for single Gaussians). In addition, we give the λ_0 , FWHM, and flux fraction for each component. We note that, excluding multiple kinematic components, DIB profiles are relatively stable other than for a few exceptions (Oka et al. 2013). Therefore, in the standard use of UNWIND (getting rid of the ISM to study the stellar spectra) we fix λ_0 , FWHM, and the flux fraction of each Gaussian component and fit just the EWs and the overall DIB velocity. The flexibility of UNWIND allows the user to modify the input DIB catalog in order to change (or fit)

the λ_0 and FWHM and to leave each component free or fixed, thus allowing it to be used as a tool to study the ISM.

B.2. A first analysis

As mentioned in the main text, the DIB catalog was built for the practical purpose of eliminating the effects of the ISM in stellar spectra. Yet, it is valuable for ISM studies. An in-depth analysis is left for future papers, here we provide a quick overview.

The new DIB catalog is more extensive in number and wavelength coverage than previous ones (Jenniskens & Desert 1994; Hobbs et al. 2008, 2009; Maíz Apellániz et al. 2015b; Fan et al. 2019; Hamano et al. 2022). The whole DIB spectrum between 4000 Å and 17 100 Å is shown in Fig. B.2. Our coverage is pretty complete in that region except for the atmospheric gaps between the *Y* and *J* and between the *J* and *H* bands and some holes in the CARMENES coverage in the near infrared. The detection threshold changes due to telluric absorption (ranging from total blockage to little or no effect, allowing for the detection of only strong DIBs in between) and S/N changes (at short wavelengths the highly extinguished stars where weak DIBs are visible are faint). Nevertheless, Fig. B.2 shows that DIBs are more common in the 5400-8000 Å range than at longer wavelengths. The situation is less clear for shorter wavelengths, as the S/N is lower and OB stars have more absorption lines that can hide weak DIBs. Narrow DIBs outnumber those with larger FWHMs but in terms of EW the situation is different, with broad and ultrabroad DIBs being more significant. In particular, broad DIBs clearly dominate the blue region but this may be partially a sensitivity issue due to the faint character of the first four standards there.

For 119 out of the 631 DIBs here we have not found equivalents in previous catalogs. The number of new discoveries is especially large in the 9800-10 900 Å (*Y* band) region, though we missed two DIBs seen by Hamano et al. (2022) because they fall on gaps of the CARMENES wavelength coverage. Among the new DIBs there are some particularly strong ones: DIBB6407 (hindered by stellar absorption in B stars but easily visible in obscured O stars), DIBB6937, DIBI8258 (both in regions of moderate telluric absorption), and DIBN11971 (coincident with a He I line, hence detected in isolation only in early-O stars).

We end up this Appendix discussing some specific DIBs.

DIBB4429. This is the most prominent broad DIB in the blue region and has been studied for a long time (Duke 1951). If one rectifies the continuum far away from the DIB itself it may be possible that the profile is a Lorentzian rather than a Gaussian (Snow et al. 2002) but such an endeavour is not practical for our primary purpose of analysing the stellar spectra. Therefore, we set the rectification points around 4400 Å and 4460 Å (the pre-

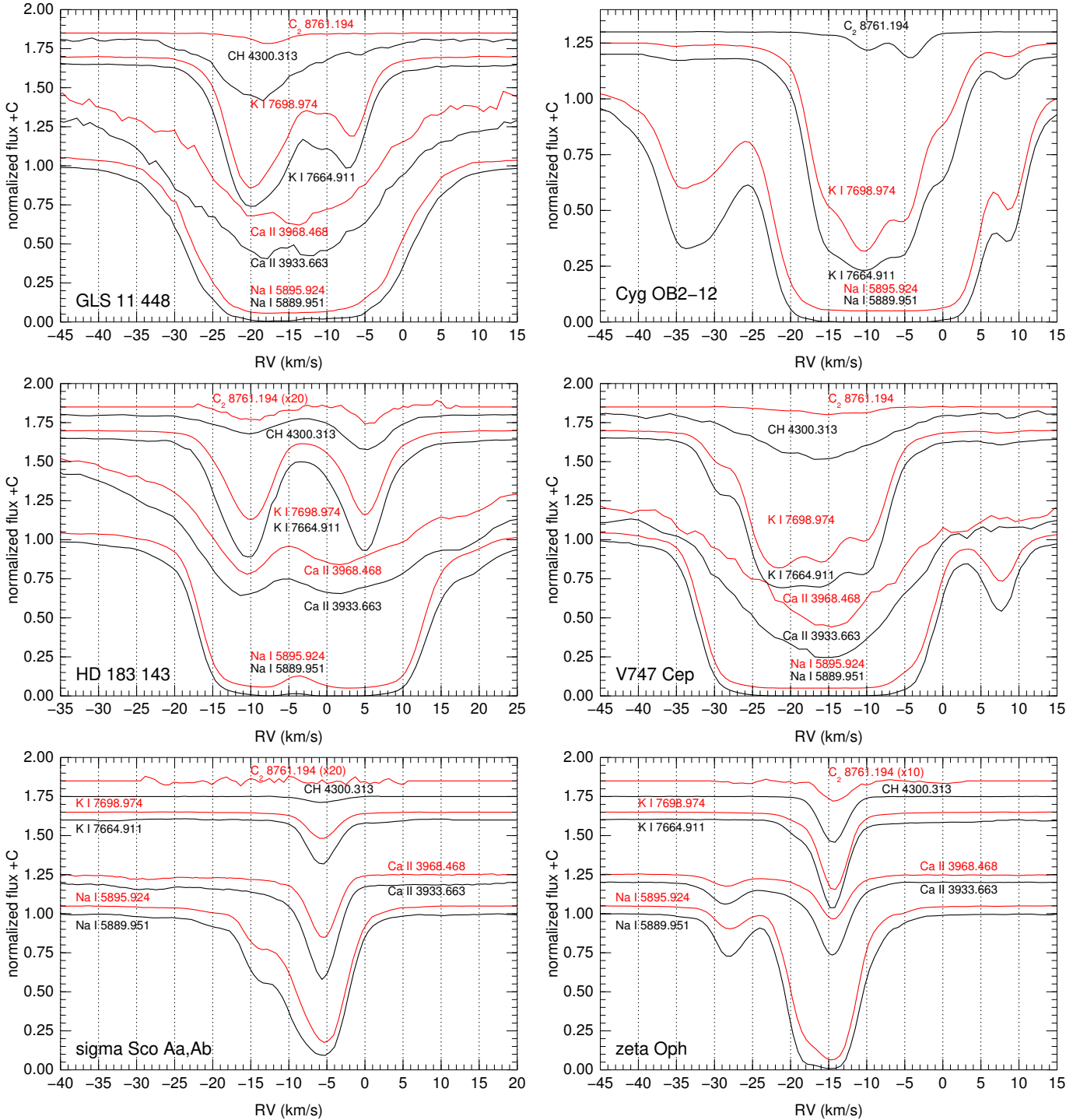


Fig. B.1. Absorption lines used to determine the ISM rest frame for the six standard stars. The Ca II lines are not available for Cyg OB2-12 in our data. The vertical scale of the $C_2 \lambda 8761.194$ line was expanded in those cases where it is weak.

cise values depending on the star) and we find, after subtracting the stellar features, that the profile is slightly asymmetric and requires two Gaussians.

DIB4884 (a.k.a. the $H\beta$ DIB). As this DIB is located right next to the (almost always present in early-type stars) $H\beta$ line, its properties are difficult to determine. We did so by forcing the stellar profile to be symmetric with respect to its central wavelength. The profile has to be fitted with two Gaussians that we combine into a single profile for convenience, as in most stars it is difficult to fit both independently with precision, but it is possible that they exhibit variations from star to star. Note, however,

than in the two relatively different sightlines of GLS 11 448 and GLS 11 449 they have EWs consistent (within the uncertainties) with the same profile (Maíz Apellániz et al. 2015b).

The 5790 Å region. This region includes the two DIBs that were first discovered, DIBN5781 and DIBN5797 (Heger 1922), and that are used as the basis for distinguishing σ and ζ sightlines. It also includes an intermediate-width DIB with typical EWs comparable to the two main ones, DIBI5778 as well as another eight weaker narrow DIBs (Fig. B.4) that should be fitted to yield accurate EWs of DIBN5781 and DIBN5797, especially at low/intermediate spectral resolutions. We fit DIBN5781 with

Table B.3. Additional information for DIBs fitted with multiple gaussians: skewness, excess kurtosis, and λ_0 , FWHM, and flux fraction for each component.

Name	λ_0 (Å)	FWHM (Å)	skew	kurt	λ_0 (Å)	FWHM (Å)	frac	Name	λ_0 (Å)	FWHM (Å)	skew	kurt	λ_0 (Å)	FWHM (Å)	frac
DIBB4429	4428.8	17.7	0.05	0.28	4427.70	9.20	0.135	DIBN9366	9365.81	2.13	-0.42	-0.40	9365.43	1.87	0.655
—	—	—	—	—	4429.00	22.70	0.865	—	—	—	—	—	9366.54	0.90	0.345
DIBN4502	4501.93	2.99	0.42	-0.42	4500.35	0.72	0.141	DIBN9429	9428.89	1.85	0.54	-0.46	9428.02	1.55	0.588
—	—	—	—	—	4501.87	2.21	0.741	—	—	—	—	—	9430.13	2.32	0.412
—	—	—	—	—	4504.20	1.35	0.118	DIBN9577	9577.41	3.33	0.54	0.02	9576.70	3.01	0.782
DIBN4727	4726.85	2.42	0.22	0.29	4726.13	0.91	0.162	—	—	—	—	—	9579.96	3.11	0.218
—	—	—	—	—	4726.99	3.99	0.838	DIBN9632	9631.94	2.37	0.29	-0.15	9631.51	1.82	0.700
DIBN4763	4762.57	2.10	-0.06	0.31	4762.54	3.00	0.875	—	—	—	—	—	9632.94	1.92	0.300
—	—	—	—	—	4762.76	0.90	0.125	DIBN9674	9673.51	1.25	0.43	-0.29	9673.16	0.75	0.538
DIBN4780	4780.44	1.56	0.39	1.25	4780.11	1.21	0.400	—	—	—	—	—	9673.91	1.07	0.462
—	—	—	—	—	4780.66	3.92	0.600	DIBN9880	9880.37	0.96	-0.25	2.44	9880.27	3.49	0.486
DIBB4884	4883.7	16.7	0.20	0.49	4880.50	9.00	0.211	—	—	—	—	—	9880.47	0.83	0.514
—	—	—	—	—	4884.60	28.60	0.789	DIBN10393	10393.31	1.07	-0.87	0.78	10392.66	1.66	0.312
DIBN5720	5719.60	0.66	0.37	-0.59	5719.39	0.59	0.706	—	—	—	—	—	10393.61	0.95	0.688
—	—	—	—	—	5720.09	0.53	0.294	DIBN10610	10610.24	1.72	-0.87	0.95	10609.48	3.11	0.400
DIBN5766	5765.91	0.74	-0.14	0.62	5765.88	1.34	0.762	—	—	—	—	—	10610.74	1.48	0.600
—	—	—	—	—	5766.00	0.45	0.238	DIBN10698	10697.61	4.41	0.14	-0.74	10696.49	2.24	0.558
DIBN5781	5780.69	2.06	0.46	0.32	5780.34	1.78	0.709	—	—	—	—	—	10698.01	0.97	0.122
—	—	—	—	—	5781.53	2.34	0.291	—	—	—	—	—	10699.21	1.48	0.276
DIBN5797	5797.23	0.70	1.11	1.98	5796.85	0.30	0.265	—	—	—	—	—	10700.73	0.70	0.044
—	—	—	—	—	5797.14	0.19	0.069	DIBN10757	10756.61	0.76	0.84	0.73	10756.39	0.65	0.625
—	—	—	—	—	5797.21	0.60	0.317	—	—	—	—	—	10756.98	1.23	0.375
—	—	—	—	—	5797.56	1.61	0.349	DIBN10781	10781.48	1.46	1.69	2.99	10780.40	1.02	0.408
DIBB6176	6176.2	23.9	0.35	-0.27	6168.60	11.50	0.306	—	—	—	—	—	10781.03	0.83	0.224
—	—	—	—	—	6179.50	21.30	0.694	—	—	—	—	—	10781.76	1.41	0.105
DIBN6203	6202.83	1.31	-0.39	-0.15	6202.57	1.24	0.583	—	—	—	—	—	10783.44	5.13	0.263
—	—	—	—	—	6203.20	0.79	0.417	DIBN10792	10792.47	1.75	0.53	-0.13	10791.96	1.33	0.630
DIBN6270	6269.83	1.27	0.13	0.98	6269.71	0.89	0.314	—	—	—	—	—	10793.34	1.82	0.370
—	—	—	—	—	6269.88	2.85	0.686	DIBN11798	11797.78	1.60	0.49	-0.00	11797.31	0.99	0.415
DIBN6284	6284.04	3.31	0.13	-0.12	6281.63	1.74	0.120	—	—	—	—	—	11798.12	1.78	0.585
—	—	—	—	—	6283.59	1.74	0.231	DIBN11971	11970.78	1.68	1.13	1.00	11970.27	1.65	0.810
—	—	—	—	—	6284.65	3.63	0.649	—	—	—	—	—	11972.95	2.37	0.190
DIBN6614	6613.71	0.96	0.52	-0.04	6613.18	0.27	0.164	DIBN12538	12538.11	3.25	0.52	0.24	12536.96	1.91	0.328
—	—	—	—	—	6613.52	0.31	0.226	—	—	—	—	—	12538.67	4.94	0.672
—	—	—	—	—	6613.85	0.22	0.075	DIBN13176	13176.29	3.89	0.66	0.36	13175.24	3.17	0.606
—	—	—	—	—	6613.94	1.04	0.535	—	—	—	—	—	13177.90	5.20	0.394
DIBN6993	6993.14	0.80	0.27	-0.16	6992.91	0.49	0.319	DIBN15612	15611.66	4.57	0.16	-0.26	15607.53	1.48	0.061
—	—	—	—	—	6993.24	0.74	0.681	—	—	—	—	—	15610.54	2.45	0.477
DIBN7224	7224.06	1.24	0.24	0.06	7223.81	0.94	0.364	—	—	—	—	—	15613.37	3.89	0.462
—	—	—	—	—	7224.20	1.32	0.636	DIBI15647	15647.3	5.2	-0.31	-0.20	15643.15	3.29	0.140
DIBN7562	7562.15	1.72	-0.01	-0.14	7560.90	0.43	0.025	—	—	—	—	—	15648.03	4.96	0.860
—	—	—	—	—	7562.18	1.71	0.975	—	—	—	—	—	—	—	—
DIBN8621	8620.99	3.99	0.57	0.39	8620.53	3.94	0.901	—	—	—	—	—	—	—	—
—	—	—	—	—	8625.15	2.98	0.099	—	—	—	—	—	—	—	—

Names are in black for narrow DIBs, in red for intermediate ones, and in green for broad ones.

two Gaussians and DIBN5797 with four, noting that the latter shows kinematic broadening in our first four standard stars.

DIBU7697. This ultrabroad band was discovered by Maíz Apellániz et al. (2021a) in HST and ground-based spectra and later confirmed by Weiler et al. (2023) using *Gaia* XP spectra. These bands are sometimes called intermediate-scale structures and several others appear to exist in the optical spectrum but those are somewhat broader and harder to detect (Zhang et al. 2024; Saydjari & Green 2025). The single-Gaussian fit yields a central wavelength of 7696.5 Å and a FWHM of 151.6 Å, the first compatible with the (vacuum) value of 7699.2 ± 1.3 Å of Maíz Apellániz et al. (2021a) but the second somewhat smaller than the 176.6 ± 3.9 Å value there. The likely explanations for that small discrepancy are the lower extinction and resolution of the original STIS data and the addition of several new DIBs in the present analysis that detract from the ultrabroad profile.

The Gaia RVS window. The 8450-8720 Å region covered by the *Gaia* RVS spectrometer (Prusti et al. 2016) has become popular for DIB studies thanks to the data availability in *Gaia* DR3, soon to increase significantly in DR4. Most such studies concentrate on the strongest DIB, DIBN8621 (e.g. Schultheis et al. 2023), with some including the second one in EW for most sightlines, DIBI8646 (e.g. Zhao et al. 2024). A third previously known DIB, DIBN8530 (Jenniskens & Desert 1994), has been ignored in recent studies to our knowledge. In addition to those, we detect three new weak DIBs close to the bluemost window limit (DIBN8456, DIBN8459, and DIBN8472, possibly excluded by the processing pipeline) and another three in the central part of the window (DIBN8571, DIBN8572, and DIBN8580, Fig. B.5). We suspect the reason they have not been discussed before despite the availability of *Gaia* data is that most current analyses in the RVS window are done with late-type stars, where

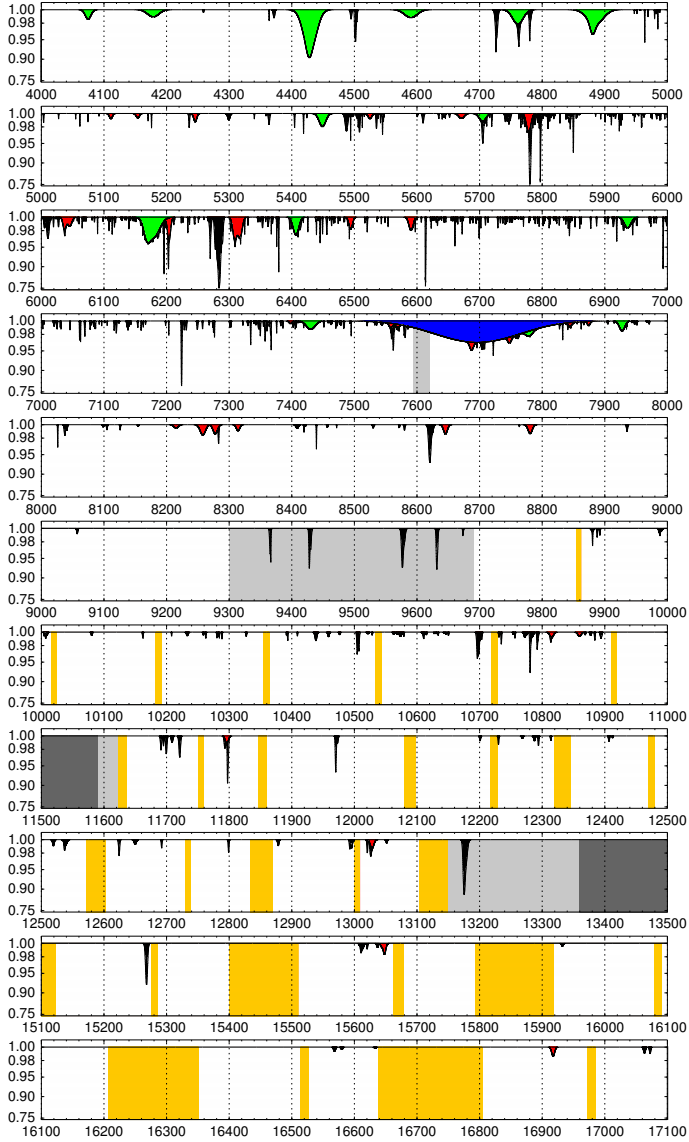


Fig. B.2. Rectified DIB spectrum for GLS 11 448. The horizontal scale is in Å and the non-linear vertical scale is used to emphasise weak DIBs. The DIB colour code is the same as in Table B.2. Light gray areas indicate where telluric absorption severely hampers the detection of DIBs and dark gray areas where it makes it impossible. Light orange areas are gaps (detectors or orders) in the CARMENES coverage.

stellar lines more easily hide ISM bands. Of the not studied ones, DIBN8530 and DIBN8580 have the best potential for detection. The well-studied DIBN8621 is clearly asymmetric in our data, a fact not considered in some of the recent studies, and has to be fitted with a double Gaussian profile that yields a significant skewness of 0.57. The intermediate-width DIBI8646 is more difficult to measure due to the presence of a nearby Paschen line.

The fullerene DIBs. DIBN9366, DIBN9429, DIBN9577, and DIBN9632 are the only four DIBs with an identified carrier, C_{60}^+ (Campbell et al. 2015). All four are in a region with severe telluric absorption, especially the first two. Nevertheless, we are able to detect them thanks to our multi-epoch technique that moves telluric lines with respect to the ISM rest frame. All four require two Gaussians due to their asymmetric nature.

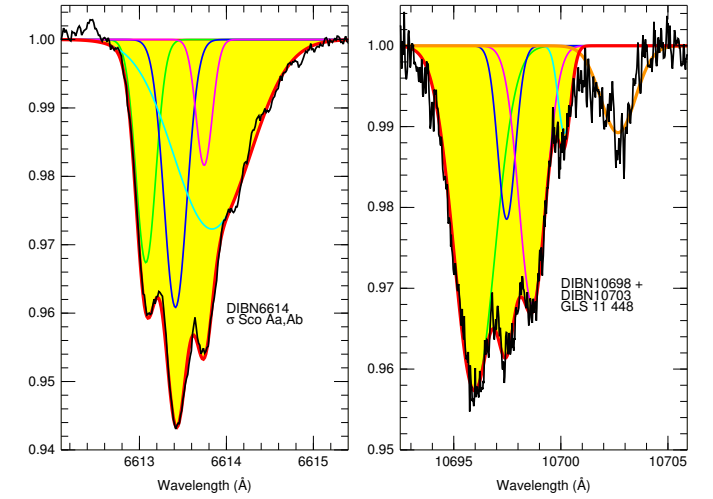


Fig. B.3. Two narrow DIBs (black) with multiple Gaussian components (in different colours) and the global fit in red filled in yellow. The right panel shows an additional DIB (DIBN10703).

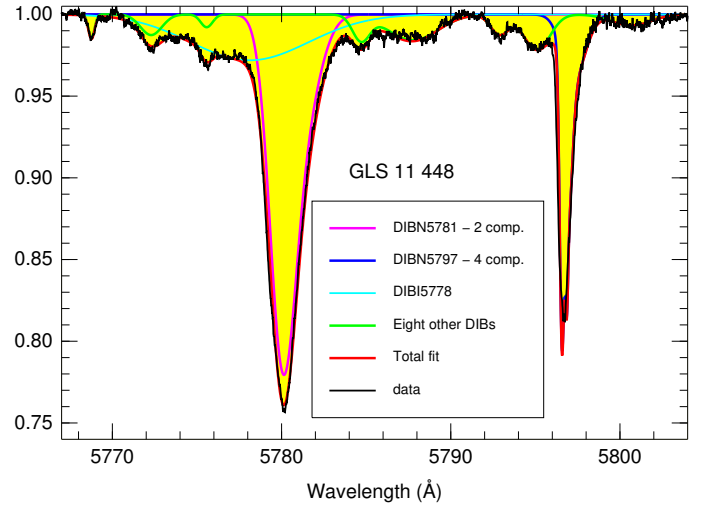


Fig. B.4. The 11 DIBs in the 5790 Å region for GLS 11 448 including the two-component DIBN5781, the four-component DIBN5797, and DIBI5778. As DIBN5797 is kinematically broadened (Fig. B.1), the data are slightly broader than the fit.

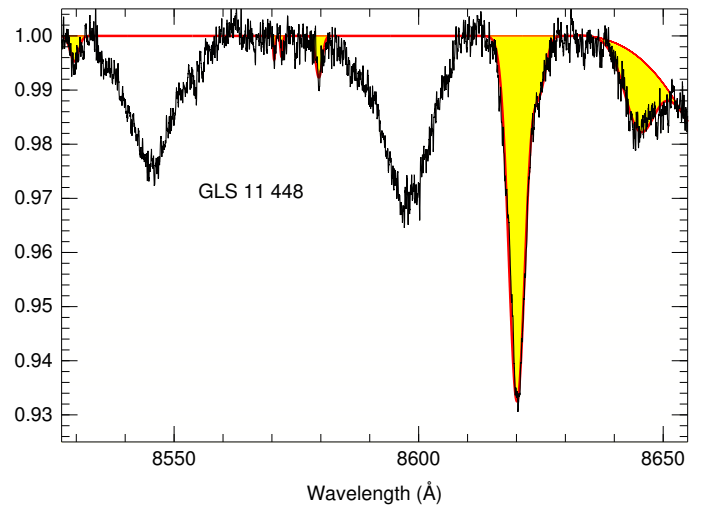


Fig. B.5. Six DIBs in the *Gaia* region for GLS 11 448 including the two-component DIBN8621 (another three weak DIBs are outside the plotted area close to the edge of the RVS window).